MECHANICAL ENGINEERING SCIENCE

ISSN:2661-4448(online)
2661-443X(print)
Volume 6 No.2 2024

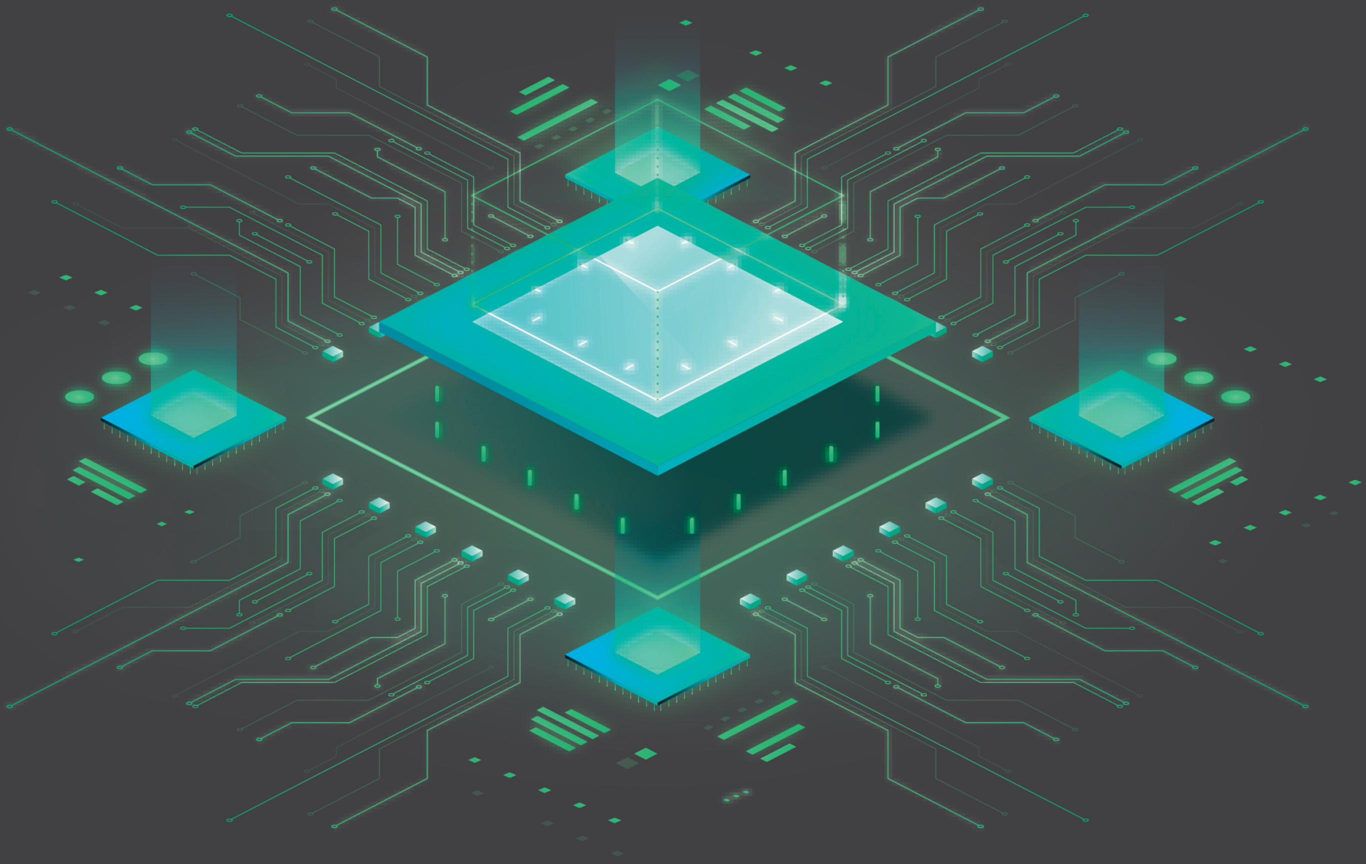

VISER
www.viserdata.com

COMPANY INTRODUCTION

Viser Technology Pte. Ltd. was founded in Singapore with branch offices in both Hebei and Chongqing, China. Viser focuses on publishing scientific and technological journals and books that promote the exchange of scientific and technological findings among the research community and around the globe. Despite being a young company, Viser is actively connecting with well-known universities, research institutes, and indexation database, and has already established a stable collaborative relationship with them. We also have a group of experienced editors and publishing experts who are dedicated to publishing high-quality journal and book contents. We offer the scholars various academic journals covering a variety of subjects and we are committed to reducing the hassles of scholarly publishing. To achieve this goal, we provide scholars with an all-in-one platform that offers solutions to every publishing process that a scholar needs to go through in order to show their latest finding to the world.

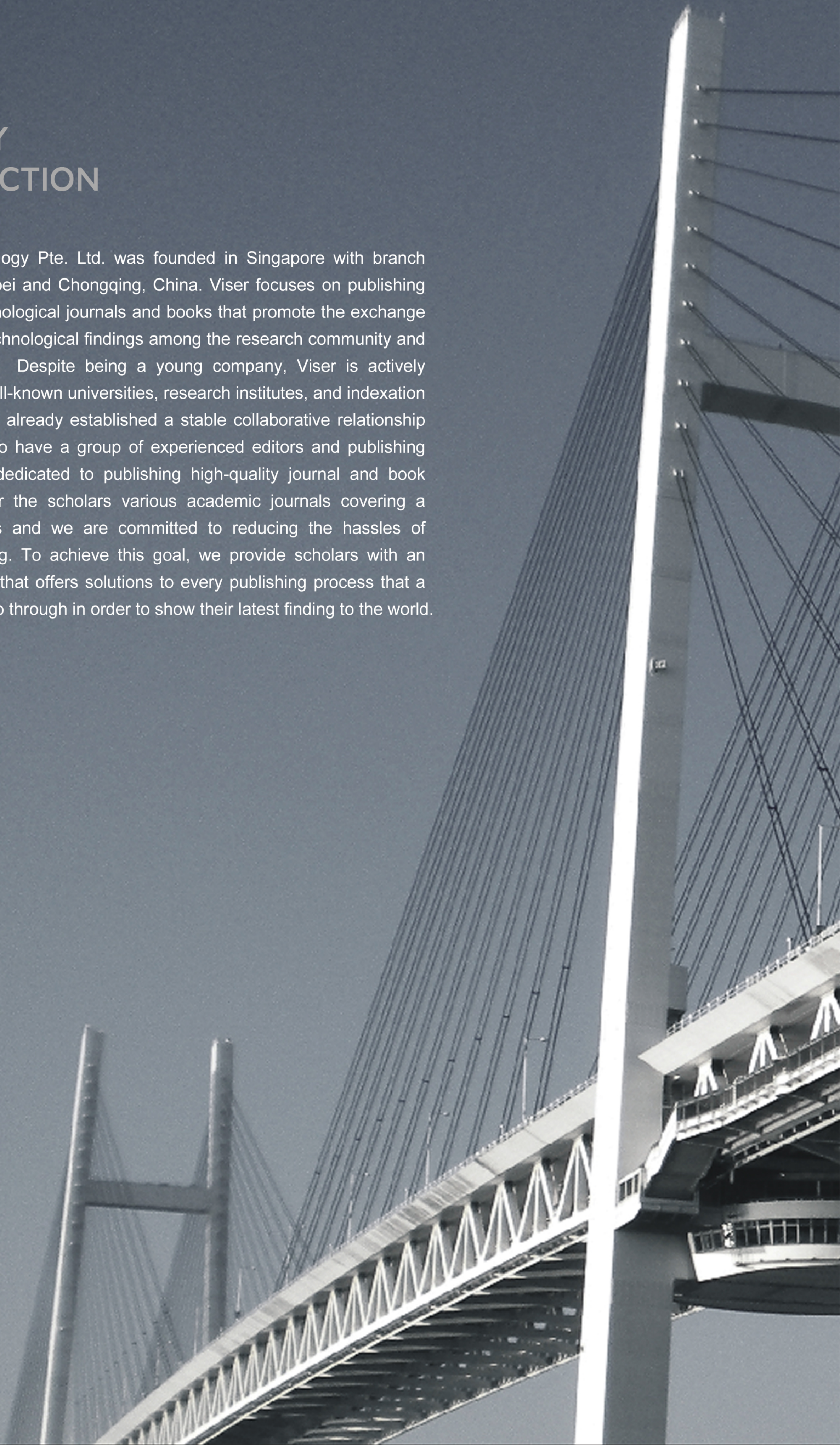

Mechanical Engineering Science

VISER

Publisher: Viser Technology Pte. Ltd.

ISSN: 2661-4448(online)

2661-443X(print)

Frequency: Semi-annual

Add.: 111 North Bridge Rd, #21-01 Peninsula Plaza,

Singapore 179098

https://www.viserdata.com/

Editors:

Yajun LIAN Yanli LIU

John WILSON Nike Yough

Mart CHEN Qiuyue SU

Debra HAMILTON Xin DI

Jennifer M DOHY Xiuli LI

Edward Adam Davis

Designer: Anson CHEE

Mechanical Engineering Science

Volume 6 No.2 (2024)

CONTENTS

VISER

Viser Technology Pte. Ltd.
Mechanical Engineering Science
DOI: 10.33142/mes.v6i2.14411

Research Article Open Access

Experimental Study of the Characteristics of Solar Cells Affected by the Angle of Incidence of Illumination

Tianlong YUAN*, Xidan ZHANG, Sitong HOU, Peng LI, Wei CONG

Liaoning Provincial Key Laboratory of Energy Storage and Utilization, Yingkou Institute of Technology, Yingkou, Liaoning, 115014, China

Corresponding Author: *Tianlong YUAN, E-mail: yuantianlong@yku.edu.cn*

Abstract

As the global energy crisis continues to intensify, the search for alternative energy sources has become increasingly urgent. As an emerging clean energy source, photovoltaic power generation not only effectively reduces carbon dioxide emissions, but also has many advantages such as renewability and distribution. Therefore, photovoltaic solar energy has attracted great attention. This article mainly studies the influence of different incident angles of light on the characteristic parameters of solar panels made of different materials under certain light intensity. Using the control variable method, under a fixed incident angle of light, the intensity of the light source irradiance is adjusted by changing the magnitude of the light source current to obtain the open circuit voltage, short-circuit current, maximum output power, and fill factor under different conditions. Use Origin software to draw characteristic curves and fit the variation pattern of photovoltaic characteristic curves. The basic characteristics of solar photovoltaic cells can be characterized by the relationship curve between their current and voltage. Finally, it is concluded that the basic characteristic parameters of solar cells increase with the increase of light intensity; When the incident angle of light is 75°, the conversion efficiency reaches its maximum.

Keywords: *solar cell; incident angle; conversion efficiency*

1 Introduction

By using the photovoltaic effect, solar cells, sometimes referred to as photovoltaic cells, transform light energy into electric energy[1]. Based on the photovoltaic effect, solar cells are conversion devices that directly transform radiant energy into electric energy[2]. The P-N junction depletion zone has a strong built-in electric field, which causes electrons and holes produced there to flow in opposite directions and exit the region due to the force of the electric field. As a result, the photo voltaic effect of the P-N junction is formed at both ends, the potential in the P region grows, and the potential in the N region falls[3].

The most commonly used solar cell today is the silicon solar cell. Silicon solar cells are large-area P-N junctions made of silicon semiconductor materials connected in series and parallel[4]. Metal grid lines are formed on the n-type material layer as contact electrodes, and metal films are also formed on the back side as contact electrodes to form a solar panel. Generally speaking, there are three types of common solar cells, the main difference is that the materials used are different, namely: monocrystalline silicon, polycrystalline silicon and amorphous silicon. Among them, the conversion efficiency of monocrystalline silicon solar cell is the highest, its actual conversion rate is about 18%, and its service life is about 20 years. It is the main component of industrial production and various large-scale production applications. Although the conversion efficiency of polysilicon solar cells is still lower than that of monocrystalline silicon solar cells in application, its conversion efficiency can also reach about 15%. In addition, compared with amorphous silicon solar cells, polycrystalline silicon solar cells are not the best choice due to their lower price, lower efficiency and short lifetime

With the rapid development of China's photovoltaic industry and the increasing penetration rate, the stability and security of the electricity market have become increasingly important. The construction of the power grid is lagging behind the construction of the power supply. However, due to the intermittency, randomness and variability of solar generation, a large amount of solar PV will be connected to the grid, bringing new demands on grid stability and energy security[5].

It is therefore necessary to find ways of improving the performance and stability of solar cells. There are many influencing factors, but the most obvious are the angle of incidence of sunlight, ambient temperature, shading, dust accumulation and so on. In this experiment, the output characteristics of solar cells are studied by selecting different angles of incidence, and at the same time, the influence of different angles of incidence on the performance of solar cells is understood, and the curves of current and voltage are constructed. In addition, it is

Received on October 13, 2024; Accepted on November 16, 2024

necessary to understand the changing laws of current and voltage emitted by solar cells at different angles of incidence. Through the relevant knowledge in the design process and the practical process of the experiment, the optimal angle of incidence of illumination is determined so that the output efficiency of the solar cell can reach the highest.

2 The Basic Principle of the Experiment

2.1 Photovoltaic effect of P-N junction

Photovoltaic power generation is based on the principle of the photovoltaic effect of the semiconductor P-N junction, which uses solar cells to convert solar energy directly into electrical energy. "Photovoltaic" refers to the phenomenon that when the target is irradiated, the distribution of charges in the target is changed, which causes electromotive force and current in the target. Photoelectric effect is a process of converting photons or light waves into electrons, and then converting light energy into electrical energy, and then voltage will be generated. Under the irradiation of light, the uneven semiconductor and the position where it is connected with the metal appear potential difference.

When the P-N junction of a semiconductor is exposed to sunlight or other radiation, a voltage is generated on both sides, known as the photovoltaic voltage. On the same silicon wafer, two types of wafers, N and P, namely P-N junctions, have been prepared on two types of semiconductors by different doping processes. Due to the existence of an electric field in the P-N junction, electrons move to the N region and holes move to the P region, so that electrons accumulate in the N region and holes accumulate in the P region, resulting in a potential difference between the two sides of the P-N junction and a photogenerated electromotive force on both sides of the P-N junction.

2.2 Main performance parameters of solar cells

(1) Short-circuit current (I_{sc}): Under the illumination condition, the output current of the solar cell is called short-circuit current if the output voltage is 0 when the two sides of the cell are short-circuited;

(2) Open-circuit voltage (U_{oc}): Under the illumination condition, the output voltage of the solar cell, if the cell is not connected to the load, its output current is 0, and the voltage at this time is called open-circuit voltage;

(3) Maximum output power (P_m): The maximum power that the panel can achieve under normal working conditions, which can be obtained by multiplying the peak current and the peak voltage. Namely: $P_m = I_m \times U_m$;

(4) Fill factor (FF): The fill factor of solar cells refers to the ratio of output voltage to output current at the maximum power point. The higher the filling factor, the better the performance of the battery, that is:

$$FF = \frac{P_m}{I_{SC} \times U_{OC}} \qquad (1)$$

(5) Conversion efficiency (η): the light energy irradiated on the battery surface is converted into electric energy:

$$\eta = \frac{P_m}{A \times P_{im}} \qquad (2)$$

Where A is the area of the battery panel, $P_{im} = 1000W/m^2 = 100mW/cm^2$.

3 Experimental Process

In this experiment, the solar panel used is made of two different materials, one is made of monocrystalline silicon, and the other is made of polycrystalline silicon. The light-receiving area of the solar panel in the experiment is 30.25 cm^2 (55 × 55mm), and the experiment is divided into two parts:

(1) Under different incidence angles, the monocrystalline silicon solar panel with a side length of 55×55mm and an area of 30.25cm2 is exposed to the sun with an incidence Angle of 90°, 75°, 60°, 45° and 30°, the experimental data are shown in Table 1, Table 2, Table 3, Table 4 and Table 5, and the changes of the test results are shown in Figure 1.

Table 1 Experimental data of monocrystalline silicon solar panel at 90 °light incidence angle

Lux(W/m^2)	U_{oc}(V)	I_{sc}(mA)	P_{max}(mW)	FF
160	2.10	20.7	31.8	0.731
220	2.12	25.8	40.9	0.748
275	2.15	31.5	51.4	0.759
350	2.17	39.7	66.1	0.767
425	2.18	49.6	83.4	0.771
510	2.18	60.3	102.0	0.776

Table 2 Experimental data of monocrystalline silicon solar panel at 75 °light incidence angle

Lux(W/m^2)	U_{oc}(V)	I_{sc}(mA)	P_{max}(mW)	FF
160	2.08	22.6	34.1	0.726
220	2.11	28.6	44.1	0.731
275	2.14	35.3	55.8	0.738
350	2.16	45.2	72.1	0.739
425	2.17	56.2	91.1	0.747
510	2.17	68.2	111.5	0.754

Table 3 Experimental data of monocrystalline silicon solar panel at 60 °light incidence angle

Lux(W/m^2)	U_{oc}(V)	I_{sc}(mA)	P_{max}(mW)	FF
160	2.07	17.9	28.4	0.766
220	2.06	24.2	38.0	0.763
275	2.09	31.2	50.2	0.770
350	2.11	39.8	65.3	0.778
425	2.14	49.6	83.2	0.784
510	2.20	59.8	103.9	0.790

Table 4 Experimental data of monocrystalline silicon solar panel at 45 ° light incidence angle

Lux(W/m^2)	U_{oc}(V)	I_{sc}(mA)	P_{max}(mW)	FF
160	2.06	15.2	22.0	0.702
220	2.07	18.1	27.4	0.731
275	2.10	22.0	34.1	0.742
350	2.12	28.0	44.6	0.752
425	2.13	34.8	56.2	0.758
510	2.14	42.2	69.1	0.765

Table 5 Experimental data of monocrystalline silicon solar panel at 30 ° light incidence angle

Lux(W/m^2)	U_{oc}(V)	I_{sc}(mA)	P_{max}(mW)	FF
160	1.94	11.4	15.6	0.705
220	1.99	14.4	20.9	0.727
275	2.00	16.4	24.0	0.732
350	2.03	20.9	31.4	0.741
425	2.06	24.8	38.5	0.754
510	2.09	28.5	45.6	0.766

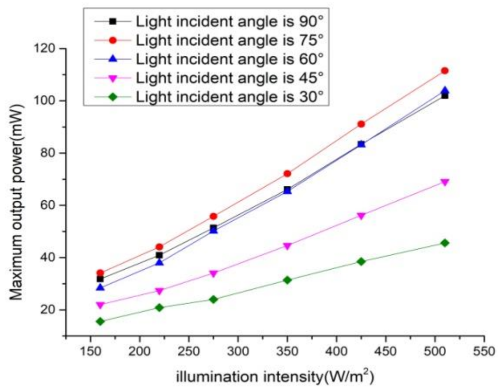

Figure 1 Illuminance of monocrystal silicon solar panels at different angles of incidence

(2) Under different incidence angles, the polysilicon solar panel with a side length of 55×55mm and an area of 30.25cm2 is exposed to the sun with an incidence Angle of 90 °, 75 °, 60 °, 45 ° and 30 °, the experimental data are shown in Table 6, Table 7, Table 8, Table 9 and Table 10, and the changes of the test results are shown in Figure 2.

Table 6 Experimental data of polycrystalline silicon solar panels at 90 ° light incidence angle

Lux(W/m^2)	U_{oc}(V)	I_{sc}(mA)	P_{max}(mW)	FF
160	3.07	10.4	21.4	0.671
220	3.10	12.7	27.1	0.689
275	3.13	15.1	32.9	0.696
350	3.17	19.2	43.3	0.712
425	3.20	23.8	55.2	0.724
510	3.26	28.6	68.6	0.736

Table 7 Experimental data of polycrystalline silicon solar panels at 75 ° light incidence angle

Lux(W/m^2)	U_{oc}(V)	I_{sc}(mA)	P_{max}(mW)	FF
160	3.07	11.9	25.6	0.702
220	3.12	14.5	33.2	0.733
275	3.14	15.8	36.8	0.743
350	3.15	20.1	47.7	0.753
425	3.18	25.1	60.1	0.753
510	3.19	30.4	73.3	0.756

Table 8 Experimental data of polycrystalline silicon solar panels at 60 ° light incidence angle

Lux(W/m^2)	U_{oc}(V)	I_{sc}(mA)	P_{max}(mW)	FF
160	2.99	10.9	22.9	0.704
220	3.02	13.2	27.9	0.670
275	3.05	15.3	33.5	0.717
350	3.09	19.7	44.3	0.728
425	3.14	24.5	56.5	0.735
510	3.26	29.5	71.7	0.746

Table 9 Experimental data of polycrystalline silicon solar panels at 45 ° light incidence angle

Lux(W/m^2)	U_{oc}(V)	I_{sc}(mA)	P_{max}(mW)	FF
160	2.99	8.9	18.9	0.710
220	3.04	10.5	23.2	0.725
275	3.06	10.9	24.2	0.724
350	3.10	14.0	31.9	0.734
425	3.13	17.7	40.8	0.737
510	3.14	21.5	50.0	0.741

Table 10 Experimental data of polycrystalline silicon solar panels at 30 ° light incidence angle

Lux(W/m^2)	U_{oc}(V)	I_{sc}(mA)	P_{max}(mW)	FF
160	2.76	6.1	10.9	0.650
220	2.83	6.7	12.6	0.664
275	2.87	6.3	11.8	0.654
350	2.93	8.2	16.2	0.675
425	3.00	10.5	21.5	0.683
510	3.10	12.7	27.7	0.704

According to the above conversion efficiency, we can see that the conversion efficiency of monocrystalline silicon solar panels is better than that of polycrystalline silicon solar panels. The reason why monocrystalline silicon solar cells have high conversion efficiency is that their silicon material crystallizes as a single crystal, with a complete crystal structure and fewer impurities, which can more effectively convert light energy into electrical energy. In contrast, polycrystalline silicon solar cells are made by mixing multiple silicon sources, and their crystal structure is not as complete as monocrystalline silicon, resulting in lower conversion efficiency.

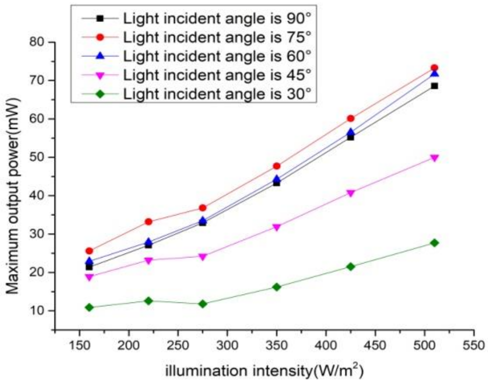

Figure 2 Illuminance of polycrystalline silicon solar panels at different angles of incidence

4 Conclusion

From the data, it can be concluded that the characteristic parameters of solar panels made of the two materials are basically the same. Under the same temperature and light intensity, the same solar panel has the maximum power output when the angle of incidence is 75, and the conversion efficiency of solar panels is the highest. Under the same temperature, light intensity and angle of incidence, the power generation efficiency of monocrystalline silicon solar panels is higher than that of polycrystalline silicon. Therefore, in order to obtain higher power generation efficiency, we should choose a monocrystalline silicon solar cell where the incident angle of light is about 75 and the illumination intensity is high.

Fund Projects: The Natural Science Foundation of Liaoning Province of China (Grant No. 2023-MSLH-314), and the 2024 Yingkou Institute of Technology Campus level Scientific Research Project (FDL202408).

References

[1] Yasurbek Gulomov, Rayimon Aliyev, Avazbek Mirzaalimov, et al. Studying the Effect of Light Incidence Angle on Photoelectric Parameters of Solar Cells by Simulation[J]. International Journal of Renewable Energy Development, 2021,10(4):731-736.

[2] Dong J, Dong Cuicui, Zhang Hongyang, et al. Energy efficiency improvement strategy of solar power generation based on photovoltaic-thermoelectric coupling method[J]. Energy and Environment, 2023,176(1):62-66.

[3] Xie N, Wang YH, He PG, et al. Principle analysis of photovoltaic effect based on silicon photovoltaic cell test data[J]. University Physics Experiment, 2022,35(6):38-42.

[4] Zhuang Guiyang, Dou Xiaoming. Policy implications and pathways for peaking carbon emissions under the new development pattern[J]. Journal of Xinjiang Normal University (Philosophy and Social Sciences Edition), 2021,42(6):124-133.

[5] Cao Wenjie. Educational research on sensor content in high school physics textbooks[D]. Suzhou: Suzhou University, 2011.

Viser Technology Pte. Ltd.
Mechanical Engineering Science
DOI: 10.33142/mes.v6i2.15052

Research Article Open Access

Experimental Study on the Performance of Plate Heat Exchangers

Tianlong YUAN, Xidan ZHANG, Sitong HOU, Peng LI, Jinguang LIANG*

Liaoning Provincial Key Laboratory of Energy Storage and Utilization, Yingkou Institute of Technology, Yingkou, Liaoning, 115014, China

***Corresponding Author:** *Jinguang LIANG, E-mail: liangjinguang@yku.edq.cn*

Abstract

The heat exchanger, a crucial device facilitating heat transfer between different temperature media, finds extensive application across diverse industries such as chemical, metallurgy, electric power, and construction, playing a pivotal role in energy conservation. It encompasses various structural configurations including tubular, shell-and-tube, and plate heat exchangers, and operates through different heat transfer modes including convection, radiation, and composite convection-radiation mecha nisms.This study focuses on experimentation with a plate heat exchanger to ascertain optimal heat transfer parameters via manipulation of heat transfer mode and flow rate. The findings underscore the significant enhancement in heat transfer efficiency achievable through judicious adjustments in working medium flow rate and heat transfer mode.

Keywords: *heat exchanger; flow rate; heat transfer mode; thermal efficiency*

1 Introduction

The heat exchanger is a device utilized to facilitate the transfer of heat between fluids at different temperatures, transferring heat from a high-temperature fluid to a low-temperature fluid in order to regulate the temperature of the fluids. It is utilized in various fields, including chemical engineering, metallurgy, electric power, and pharmaceuticals[1]. Heat exchangers are widely used in air separation units, petroleum refining, refrigeration engineering, and other fields, making them one of the most important pieces of process equipment in the chemical industry. The development of heat exchangers represents a significant technological advancement, as it can enhance energy utilization efficiency and reduce energy waste[2]. Two common types of heat exchangers are shell-and-tube heat exchangers and plate heat exchangers, each with its own advantages and disadvantages and suitable for different scenarios. Shell-and-tube heat exchangers facilitate heat exchange between fluids inside and outside the tubes, featuring a simple structure and long service life, albeit with a relatively smaller heat exchange surface area. On the other hand, plate heat exchangers consist of multiple thin plates for heat exchange between fluids in the gaps between the plates, offering a larger heat exchange surface area but requiring specialized technical personnel for operation and being more susceptible to factors such as contaminants. When selecting an appropriate heat exchanger, comprehensive considerations based on diverse application fields, process conditions, and fluid characteristics are necessary to achieve optimal heat transfer efficiency.

This study examines the impact of varying fluid flow velocities on heat exchanger performance. By conducting a comparative analysis of experimental data, it aims to identify the optimal flow pattern and velocity conducive to efficient heat exchange.

2 Experimental Principle

In order to investigate the impact of flow velocity on the performance of a heat exchanger, we selected a shell-and-tube heat exchanger for experimentation and conducted performance tests. During the experiment, we measured parameters such as actual heat transfer efficiency, logarithmic mean temperature difference, and overall heat transfer coefficient to examine the influence of different flow velocities and flow patterns on the heat exchanger's performance[3]. These parameters serve as fundamental physical quantities that characterize the heat exchanger's performance. Through the calculation of their relationships, we can gain a comprehensive understanding of the heat exchanger's working principle and performance, which will establish a solid foundation for subsequent experimental analysis and conclusions[4].

(1) The heat released by hot water.

$$Q_{heat} = G_{heat} C_{p,heat} (t_{h1} - t_{h2}) \tag{1}$$

(2) The heat absorbed by cold water.

$$Q_{cold} = G_{cold} C_{p,cold} (t_{c2} - t_{c1}) \tag{2}$$

In the formula: G_{heat} ——the mass flow rate of hot

Received on September 11, 2024; Accepted on October 27, 2024

water, kg/s;

G_{cold} ——the mass flow rate of cold water,kg/s;

$C_{p,heat}$——the specific heat of hot water at constant pressure, kJ/(kg·℃);

$C_{p,cold}$ ——the specific heat of cold water at constant pressure, kJ/(kg·℃);

t_{h1}——the inlet temperature of the hot water, ℃;

t_{h2}——the outlet temperature of hot water,℃;

t_{c1}——the inlet temperature of the cold water,℃;

t_{c2}——the outlet temperature of cold water,℃。

(3) Regardless of whether it is downstream or upstream, the logarithmic mean temperature difference can be used. The formula for this is as follows:

$$\Delta t = \frac{\Delta t_{\max} - \Delta t_{\min}}{\ln \dfrac{\Delta t_{\max}}{\Delta t_{\min}}} \tag{3}$$

Δt_{max}——Temperature difference between the inlet temperature of the heat source and the outlet temperature of the cold source;

Δt_{min} —— Temperature difference between the outlet temperature of the heat source and the inlet temperature of the cold source.

(4) The average of the heat released by hot water and the heat absorbed by cold water is taken as the heat flux of the entire heat transfer surface.

$$Q = \frac{Q_{heat} + Q_{cold}}{2} \tag{4}$$

(5) Heat transfer coefficient equation

$$K = \frac{Q}{A\Delta t_m} \tag{5}$$

(6) Heat Transfer Efficiency

$$\varphi = \frac{Q_{cold}}{Q_{heat}} \tag{6}$$

3 Experimental Data

In the experiment, the temperatures of the cold water tank and the hot water tank were maintained at a constant level. Only the flow patterns and flow rates of the hot and cold fluids were altered in order to examine their impact on the performance of the heat exchanger. Parameters such as the inlet and outlet temperatures of the cold and hot fluids were measured to evaluate the effectiveness of the plate heat exchanger. Experimental data for both co-current and counter-current flow configurations are presented in Tables 1 and 2, respectively.

4 Data of Experimental

The heat transfer efficiency diagram for parallel flow in plate heat exchangers is depicted in Figure 1, whereas for counterflow, it is illustrated in Figure 2.

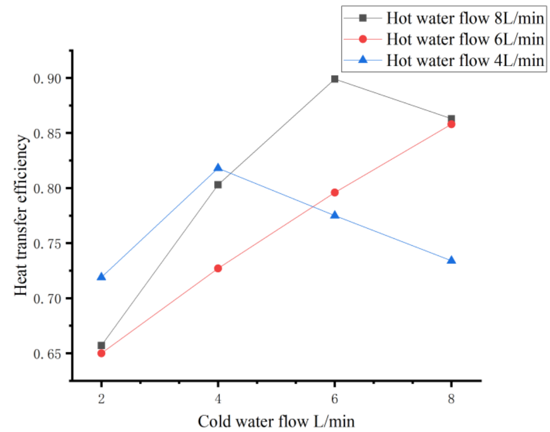

Figure 1 Illustrates the heat transfer efficiency of the parallel flow plate heat exchanger

Table 1 Experimental Data for Parallel Flow Heat Exchanger

The flux of hot water(L/min)	The flux of cold water (L/min)	The imported temperature of the hot water (℃)	The outlet temperature of hot water (℃)	The imported temperature of the cold water (℃)	The outlet temperature of cold water (℃)	The heat released by hot water (W)	The heat obtained by cold water (W)	Heat exchange efficiency	Logarithmic mean temperature difference (℃)	Heat Transfer (W)	Heat Transfer Coefficient W/(m^2 K)
8	2	50.2	40.3	14.3	40.3	5518	3623	0.657	16.67	4570	1904
8	4	50.2	37.5	14.3	34.7	7079	5686	0.803	19.09	6383	2322
8	6	50.2	35.6	14.3	31.8	8139	7316	0.899	19.81	7728	2709
8	8	50.1	34.0	14.3	28.2	8975	7748	0.863	20.78	8362	2794
6	2	50.2	38.1	14.3	37.9	5059	3289	0.650	17.42	4174	1664
6	4	50.0	34.5	14.3	31.2	6480	4710	0.727	19.49	5595	1994
6	6	50.3	33.1	14.3	28.0	7191	5727	0.796	20.50	6459	2188
6	8	49.2	31.5	14.3	25.7	7400	6355	0.858	20.19	6878	2366
4	2	50.1	35.7	14.3	35.0	4013	2884	0.719	18.07	3449	1325
4	4	50.2	32.6	14.3	28.7	4906	4013	0.818	19.86	4460	1559
4	6	50.4	29.3	14.3	25.2	5881	4557	0.775	19.66	5219	1843
4	8	50.2	27.6	14.3	22.6	6299	4626	0.734	19.59	5463	1936

Table 2 Experimental Data for Counterflow Plate Heat Exchanger.

The flux of hot water (L/min)	The flux of cold water (L/min)	The imported temperature of the hot water (°C)	The outlet temperature of hot water (°C)	The imported temperature of the cold water (°C)	The outlet temperature of cold water (°C)	The heat released by hot water (W)	The heat obtained by cold water (W)	Heat exchange efficiency	Logarithmic mean temperature difference (°C)	Heat Transfer (W)	Heat Transfer Coefficient W/(m^2 K)
8	2	50.1	38.9	13.7	45.8	6244	4473	0.716	11.82	5358	3148
8	4	50.1	36.1	13.7	39.7	7805	7274	0.929	15.64	7540	3347
8	6	50.1	34.5	13.7	33.8	8696	8403	0.966	18.45	8550	3217
8	8	50.0	32.8	13.7	29.7	9588	8919	0.930	19.69	9254	3263
6	2	50.1	36.5	13.7	44.6	5686	4306	0.757	12.16	4996	2853
6	4	50.1	34.1	13.7	36.7	6689	6410	0.958	16.66	6550	2730
6	6	50.1	31.2	13.7	32.0	7902	7651	0.968	17.80	7777	3033
6	8	50.0	29.9	13.7	27.2	7860	7525	0.957	19.31	7693	2766
4	2	50.0	33.0	13.7	42.1	4738	3958	0.834	12.76	4348	2366
4	4	50.0	28.6	13.7	33.6	5964	5546	0.930	15.63	5755	2556
4	6	50.2	26.4	13.7	29.0	6633	6396	0.965	16.58	6515	2728
4	8	50.0	27.2	13.7	24.7	6355	6132	0.964	18.79	6244	2307

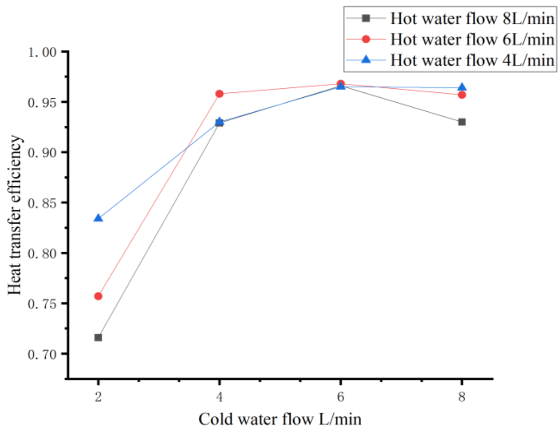

Figure 2 Heat Transfer Efficiency of Plate Heat Exchanger under Counterflow

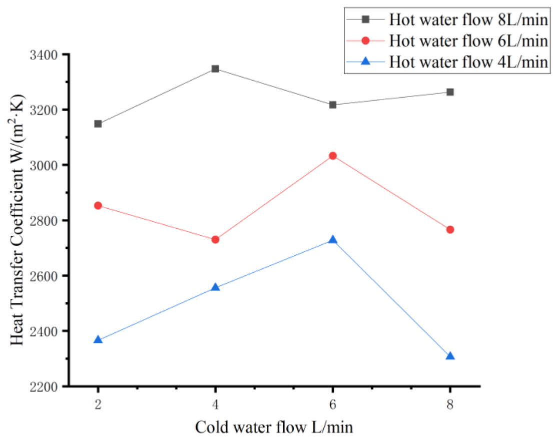

Figure 4 Depicts the heat transfer coefficient of plate heat exchangers under countercurrent flow

The heat transfer coefficient diagram for parallel flow in a plate heat exchanger is shown in Figure 3, and the heat transfer coefficient diagram for counterflow is shown in Figure 4.

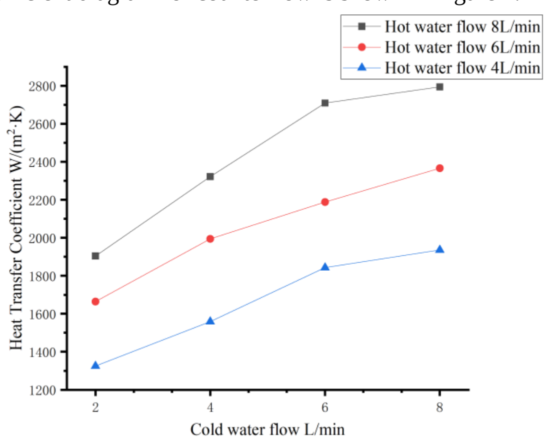

Figure 3 Illustrates the heat transfer coefficient of the parallel flow plate heat exchanger

5 The Conclusion of Data Analysis

(1) In the realm of thermal dynamics, it is a well-established phenomenon that in instances where the flow rates of hot water and cold water are disparate, counterflow operation typically exhibits a higher heat transfer efficiency compared to cocurrent operation. This superiority stems from the counterflow arrangement, wherein the direction of heat conduction opposes that of fluid flow. Consequently, this configuration facilitates a more thorough transfer of heat to the opposing fluid, thereby enhancing overall heat transfer efficiency.

(2) Optimal performance under cocurrent operation is observed when both hot and cold water flow rates are maintained at 4.0L/min. However, as the hot water flow rate escalates to 6.0L/min, the heat transfer efficiency exhibits an incremental rise with an increase in the cold water flow rate. Upon further escalation of the hot water flow rate to 8.0L/min, the heat transfer efficiency attains its zenith at a cold water

flow rate of 6.0L/min. Experimentally, it has been substantiated that the pinnacle of overall heat transfer efficiency in cocurrent operation is achieved at a hot water flow rate of 8.0L/min concomitant with a cold water flow rate of 6.0L/min. Conversely, under counterflow operation conditions, optimal heat transfer efficiency is solely realized at a hot water flow rate of 6.0L/min.

(3) Experimental observations elucidate that within cocurrent operation, the heat transfer coefficient exhibits a gradual augmentation in tandem with escalating flow rates of both hot and cold water. In contrast, counterflow operation typically manifests a higher heat transfer coefficient than its cocurrent counterpart. Nevertheless, an intriguing deviation arises as the cold water flow rate surpasses a certain threshold; rather than a continued ascent, the heat transfer coefficient undergoes a diminution.

6 Conclusion

Through calculation and analysis, it was determined that counterflow operation yields the most favorable outcomes in heat exchanger operation. This superiority primarily stems from the oppositional alignment between heat conduction and fluid flow direction in counterflow operation. Such a configuration facilitates more comprehensive heat transfer to the opposing fluid, thereby optimizing the overall heat transfer efficiency of the exchanger. Generally, counterflow exhibits heightened heat transfer efficiency, often resulting in a higher outlet temperature for the hot water compared to the cold water outlet temperature in counterflow experiments.

Fund Projects: Yingkou Institute of Technology campus level research project--- Development of food additive supercritical extraction equipment and fluid transmission system research.

References

[1] Zhao Liang. On the current research status and prospects of domestic heat exchangers[J]. Science and Wealth, 2018(2):267.

[2] Wang Peng. Analysis of the Path of Transformation and Development of China's Manufacturing Industry - Based on the Perspective of International Trade[J]. China Economic and Trade Guide, 2020,25(2):41-42.

[3] Xiao Yingzhao, Li Geqin. On the Diplomatic Policy of the Federal Republic of Germany during the Middle East Energy Crisis of the 1970s [J]. Theoretical Monthly, 2004(2):115-116.

[4] Sun Tongtong. Research Status and Application Progress of Heat Exchangers[J]. Modern Manufacturing Technology and Equipment, 2019(6):164-165.

Viser Technology Pte. Ltd.
Mechanical Engineering Science
DOI: 10.33142/mes.v6i2.15053

Research Article Open Access

Research on the Motion Characteristics of Suction Valve Plate Based on Fluid Structure Coupling

Chuncong BAI, Guangchen XU*, Huiyan ZHAO
Yingkou Institute of Technology, Yingkou, Liaoning, 115014, China
***Corresponding Author:** *Guangchen XU, E-mail: kanu012@163.com*

Abstract
The air valve is the core component of the cyclic operation of the compressor cylinder, and its structure and performance largely determine whether the reciprocating compressor can operate more efficiently and economically. On the basis of analyzing the basic structure and working principle of the air valve, this article mainly studies the motion characteristics of the suction valve plate. Based on fluid structure coupling mechanics and using ADINA software as a platform, numerical simulation analysis was conducted on the suction valve of a certain compressor model. Studying the stress of the valve plate and the variation of its upper and lower surface pressure with the opening and closing of the valve plate during the suction process of the compressor provides theoretical guidance for the rationality of the design of the air valve and related components, thereby improving the service life of the air valve and the working efficiency of the compressor.
Keywords: *reciprocating compressor; fluid structure coupling; tongue spring valve; motion characteristics*

1 Introduction

The air valve is the most critical component of a piston compressor, and its performance directly affects the energy efficiency of the compressor. A good design can reduce the flow resistance loss to as low as 3% to 7% of the compressor shaft power, and vice versa, it can reach as high as 15% to 20% of the shaft power[1]. The tongue spring valve is widely used in the design of air valves for small and medium-sized piston compressors due to its simple structure and small clearance volume. Wu Danqing[2] systematically introduced the basic mathematical model of tongue spring valve kinematics, studied key parameters such as flow coefficient and thrust coefficient of the valve plate that affect the efficiency of the gas valve, and conducted mathematical simulations of the motion law of the refrigeration compressor gas valve in reference[3]. These studies mostly focused on theoretical or fluid and structural research. This article is based on ADINA software for fluid structure coupling bidirectional simulation analysis, providing a reference basis for the further optimization design of the gas valve.

2 Structural Principle and Motion Law of Suction Valve

The suction valve is usually installed on a valve plate, and the typical structure mainly consists of two main components: the valve seat and the valve plate, as shown in Figure 1. The main function of the valve seat is to determine the opening and closing of the suction channel of the gas valve together with the valve plate, and it is the main pressure bearing component for the pressure difference inside and outside the cylinder of the reciprocating compressor; The valve disc is an opening and closing element, with one end fixed on the valve seat and the other end able to move up and down.

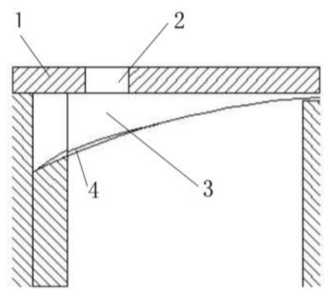

Figure 1 Inhalation valve group

1 valve seat 2 valve seat flow section 3 valve clearance flow section 4 valve disc

At present, most of the air valves used in reciprocating compressors are automatic valves. During the opening and closing process of the valve plate, the fluid pressure on both sides and the spring force on itself affect each other's dynamic changes, which are difficult to measure in experiments. Therefore, it is necessary to conduct transient simulation analysis of the compressor working process.

Received on September 12, 2024; Accepted on November 1st, 2024

3 Establishment and Solution of Finite Element Model

According to the operating principle of the compressor working mechanism, the reciprocating process of the working fluid flowing through the valve port into the cylinder from the gas chamber is regarded as the fluid region, and the valve components are regarded as the structural region. Fluid modeling and structural modeling are carried out in the ADINA-AUI module, and then relevant parameters and boundary conditions are set in the ADINA-CFD module and ADINA-Structures module respectively. Finally, the functions of ADINA-Structures and ADINA-CFD are integrated in the ADINA-FSI module to achieve coupling solution analysis between the fluid model and the structural model[4].As shown in Figure 2 and 3.

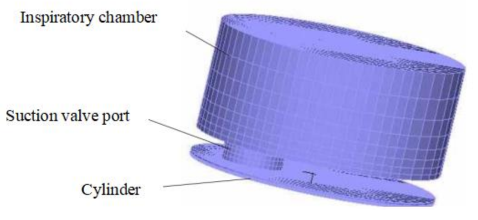

Figure 2 Fluid Model

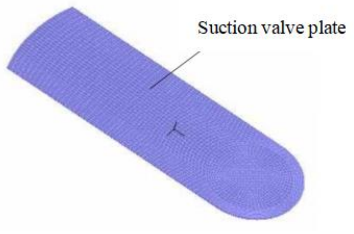

Figure 3 Structural Model

4 Pressure Characteristics of Valve Disc

4.1 Surface pressure of suction valve plate

The piston of a reciprocating compressor moves from the top dead center of the cylinder to the bottom dead center, completing the process of refrigerant gas expansion and suction. The suction valve undergoes a "close open close" cycle to complete a work cycle mission. The piston of a reciprocating compressor moves from the bottom dead center of the cylinder to the top dead center to complete the process of refrigerant gas compression and exhaust, and the exhaust valve undergoes the same opening and closing process. During the opening and closing process of the valve plate, the fluid pressure on both sides and the spring force on itself affect each other's dynamic changes, which are difficult to measure in experiments. Therefore, it is necessary to conduct transient simulation analysis on the working process of the compressor[5].

4.1.1 Analysis of surface pressure of suction valve plate

(1)Lift of suction valve plate.As shown in Figures 4 and 5, the lift curve and corresponding cylinder pressure curve of the suction valve plate with a speed of 1450r/min and a thickness of 0.635mm are presented.

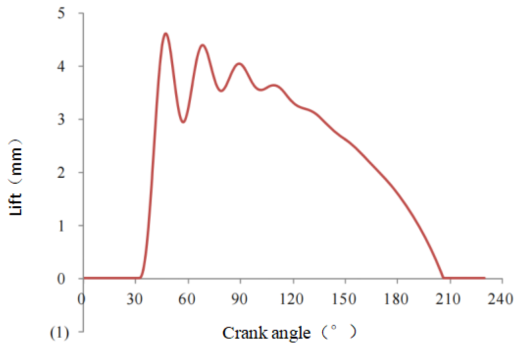

Figure 4 Valve lift curve

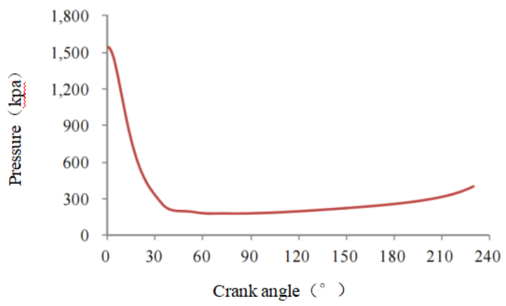

Figure 5 Cylinder pressure curve

The displacement (lift) of the valve plate in a reciprocating compressor is generated by the combined action of the pressure difference on both sides of the valve plate and its own spring force. The dynamic gas force generated by the pressure difference on both sides of the valve plate changes over time. The pushing effect of the dynamic gas on the valve plate when passing through the valve gap will cause rapid changes in the pressure and displacement it experiences. During the suction process of the compressor, as the lift of the suction valve increases, the deformation of the valve plate increases and the spring force increases. At the same time, the flow section of the valve gap increases, the decrease in cylinder pressure slows down, and the pressure difference on both sides of the valve plate decreases. When it reaches a certain degree, the valve plate will inevitably experience rebound; When the rebound lift of the valve plate decreases, the deformation decreases, the spring force decreases, and the valve clearance flow section decreases, the cylinder pressure drop increases, the pressure difference on both sides of the valve plate increases, and then the valve plate rises again. Therefore, when the suction valve plate reaches the maximum lift position, there will be a phenomenon of reduced amplitude fluctuation, and then the cylinder pressure changes relatively steadily, and the valve plate also lands smoothly.

(2) Surface pressure characteristics of valve discs.The movement of the valve plate is mainly controlled by the pressure difference generated on both sides of the valve plate and its own spring force. When the combined force of dynamic gas forces on the upper and lower sides of the suction valve plate is upward, the valve plate is obstructed and in a relatively static state; When the combined force of dynamic gas forces on both sides of the valve plate is downward and greater than the valve plate's own elasticity, the valve plate moves downward. Conversely, when the combined force is downward and less than the valve plate's own elasticity, the valve plate rebounds upward. It is evident that the pressure difference on both sides of the valve plate plays an important role in the entire working process, so it is necessary to analyze the pressure distribution on both sides of the valve plate. As shown in Figure 6, the pressure cloud map of the upper and lower surfaces of the suction valve at the moment of just opening, half opening, full opening, half closing, and about to close (corresponding crank angles are shown in Table 1) is shown. The left column shows the pressure cloud map of the upper surface of the valve plate, and the right column shows the pressure cloud map of the lower surface.

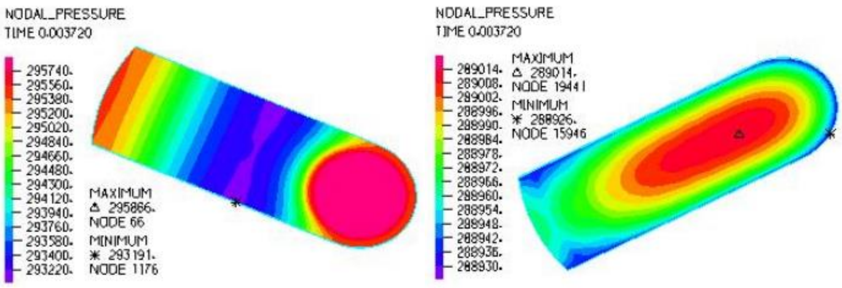

Just opened

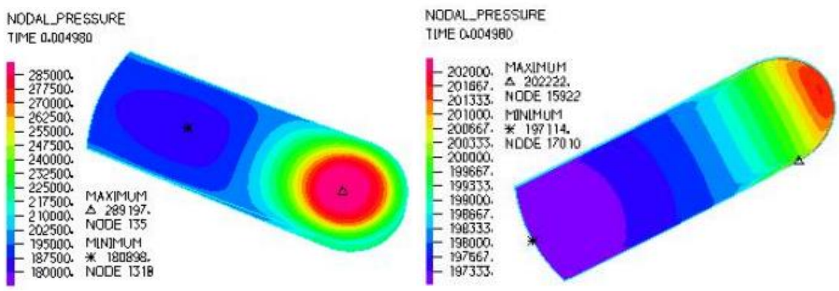

Half opened

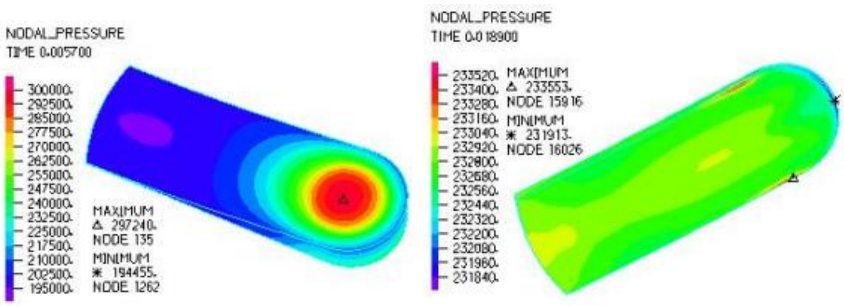

Fully opened

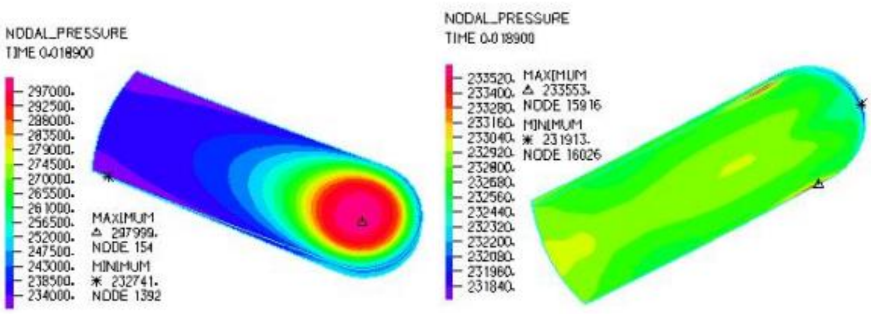

Half closed

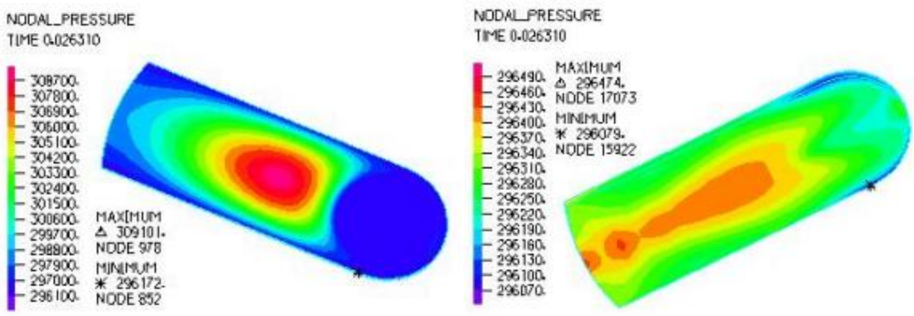

Close All

a) Upper surface of valve disc　　b) Lower surface of valve disc

Figure 6 Surface pressure cloud map of suction valve plate

From the above figure, it can be seen that when the suction valve is just opened, the valve clearance flow section is very small, and the gas flow resistance is large. A large high-pressure area appears at the top of the valve surface. At the same time, due to the structural form of the valve root, the gas flow is obstructed, resulting in a slightly higher gas pressure at the root than in the middle of the valve. The gas flow form of the tongue spring valve component causes a higher gas flow velocity and lower pressure in the outer ring on the lower surface of the valve; When the valve disc rises to half open, the lift of the valve disc increases, the effective flow cross-section increases, and the pressure on the upper surface is mainly concentrated in the head area of the valve disc corresponding to the valve port. The range of the high-pressure zone is reduced, and a high-pressure zone appears at the forefront of the lower surface; When the valve plate reaches the maximum lift position, the air flow rate reaches its maximum, and the high pressure area on the upper surface is more concentrated. Due to the influence of the tongue spring automatic valve structure on the flow pattern of the working fluid, the pressure on the lower surface of the valve plate decreases from the head to the root; When the valve disc falls back to half closed, the flow resistance increases again, the high-pressure zone on the upper surface increases, the pressure at the root of the lower surface decreases, and the overall pressure is relatively balanced. A medium and high-pressure zone appears on the side of the valve disc; When the valve disc is about to close, due to the upward movement of the piston after the crank angle exceeds 180° and the small lift, the pressure on the surface of the valve disc facing the valve port first decreases, and the pressure center shifts towards the middle of the valve disc. The valve clearance quickly decreases, causing the pressure on the lower surface of the valve disc near the root to slightly increase. In order to have a clearer understanding of the surface load changes during the movement of the valve plate, the maximum surface pressure and corresponding rotation angles of the valve plate are recorded in Table 1 and Figure 7(the relationship between the movement status of the suction valve plate and the corresponding rotation angle is set in this way, unless otherwise emphasized in the following text).

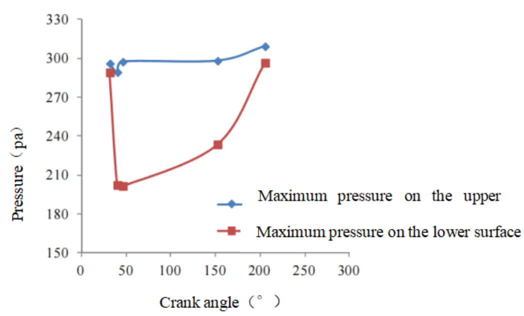

Figure 7 Maximum pressure on the surface of the suction valve plate

As shown in the above figure, as the valve plate rises and falls, the maximum pressure on the upper surface of the suction valve plate fluctuates slightly and remains basically constant. The maximum pressure on the lower surface decreases with the opening of the valve plate and increases with the falling back of the valve plate. Therefore, the pressure difference between the upper and lower surfaces increases with the opening of the valve plate and decreases with the falling back.

Table 1 Maximum pressure on the upper and lower surfaces during the movement of the suction valve plate

Sports state	Just opened	Half opened	Fully opened	Half closed	Close all
Corresponding angle(°)	31.89	40.39	46.28	152.23	205.42
Upper surface pressure(pa)	295866	289197	297240	297999	309101
Lower surface pressure(pa)	289014	202222	201462	233553	296474

5 Conclusion

Using ADINA's fluid structure coupling technology, simulate the motion law and gas flow state of the valve plate, analyze the self stress and flow field changes on both sides during the valve plate motion process. The research results indicate that during the suction process, the opening time of the valve plate is relatively long during the cycle, and there is a large fluctuation in the initial stage of reaching the maximum lift. The high stress area of the valve plate is always concentrated at the root of the valve plate, and the upper surface pressure slightly increases and remains basically constant. The lower surface pressure decreases with the opening of the valve plate and increases with the falling of the valve plate. The pressure difference on both sides of the valve plate and its maximum stress also increase with the opening and decrease with the falling of the valve plate. When the valve plate moves to the highest lift position, the stress extreme value of the valve plate is maximum.

Reference

[1] Wang Y, Xue C,Feng J, et al. Experimental investiga- tion on valve impact velocity and inclining motion of a re-ciprocating compressor[J]. Applied Thermal Engineering, 2013,61(2):149-156.

[2] WU Danqing. Study ofthe effective flow area and the flow coefficient of the reed valve in compressor[J]. Fluids Engineering, 1984,12(10):37-41.

[3] WANG Yi, TAN Weihua. Mathematical simulation of valve movement for refrigeration compressor[J]. Journal of Fluids Machin-ery, 2001,29(3):18-22.

[4] Bai Chuncong. Numerical simulation analysis of reciprocating compressor tongue spring valve based on fluid structure coupling[D]. Liaoning: Dalian Jiaotong University, 2017.

[5] Wang Li, Liu Zhenquan, Hu Songcheng. Research on the influence of dynamic gas force on the motion law of reciprocating compressor valve[J]. Gansu Science and Technology, 2009(3):55-57.

Viser Technology Pte. Ltd.
Mechanical Engineering Science
DOI: 10.33142/mes.v6i2.15054

Research Article Open Access

Design of Plastic Injection Mold with Support Strip Based on CAD/CAE

Wenwu ZHANG, Guangchen XU*

Yingkou Institute of Technology, Yingkou, Liaoning, 115017, China

***Corresponding Author:** *Guangchen XU, E-mail: kanu012@163.com*

Abstract

The structural characteristics of plastic parts containing support strips were analyzed, and Moldflow software was used to simulate and analyze the pouring position and cooling system of the plastic parts to determine the optimal solution. The UG-Moldwizard module was used to complete the mold base design of the injection mold, which reduced the potential risks in the design of the injection mold, improved the quality of the mold, and reduced the number of mold trials. It fully demonstrated the role of CAE technology in the design of the pouring system and the development process of the injection mold. The outstanding role it plays in the process can provide reference value for the design of injection molds similar to plastic parts.

Keywords: *CAD; CAE; injection mold; support strip*

1 Introduction

With the widespread application of injection molded products, their shapes and structures are becoming more and more complex, and their appearance requirements are also increasing.Traditional two-dimensional mold design and processing methods cannot meet the needs of modern and integrated production. The use of advanced mold CAD/CAE technology can assist in determining the gating system,predicting product defects,and optimizing process parameters during processing. It can shorten the molding cycle and reduce the defective rate of plastic parts[1].Siemens' large-scale interactive CAD/CAM software UG NX is widely used in the mold industry. Its injection mold wizard module Mold wizard provides a professional injection mold design platform. The mold parting tool is powerful and easy to operate[2]. Autodesk's Moldflow software can realize injection molding process analysis. This software has been dominating the plastic molding analysis market with its powerful CAE analysis capabilities. It can realize data exchange between systems with UG NX through standard output formats such as IGES and STL.

Plastic parts containing support strips are increasingly used in automotive,military, aerospace and other fields. This type of parts can improve the strength and stiffness of the parts while reducing the overall mass to meet lightweight requirements. Currently, there is little literature on the design of injection molds for plastic parts with support strips. Therefore, this article takes the mold design of support strip plastic parts as the main line, combines injection molding CAD/CAE technology, and explains the molding process analysis and mold design method of support strips.Its design ideas can provide useful reference for similar molds.

This article uses the UG Mold wizard module and Moldflow software as assistance to optimize injection mold design and process parameters, solving the production method of only obtaining the final result through repeated trial and error, mold repair, and parameter adjustment in the design and manufacturing process of support bar injection molds, and improving the quality and production efficiency of plastic products.

2 Plastic Part Structure Analysis

The three-dimensional model of the plastic part is shown in Figure 1. Its overall size is 150mm×50mm×65mm, the volume is 48cm^3, the average wall thickness is 2mm, and The material used is acrylonitrile butadiene styrene copolymer (ABS) from Kumho company in Moldflow database, with the grade HFA 700 and a shrinkage rate of 0.5%. There are support strips in the middle of the plastic part, and their position distribution meets the requirements of structural mechanics; There are concavities at the

Received on September 23, 2024; Accepted on November 5th, 2024

round cones on both sides, and a side core-pulling structure needs to be designed.There are precision requirements for the fitting of plastic parts, requiring mass production, and the surface must be free of shrinkage holes, flash and burrs.

Figure 1 3D model of plastic part

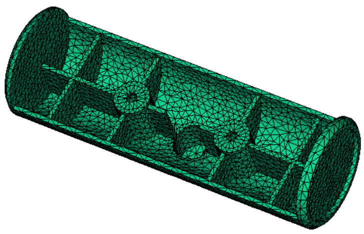

Figure 2 Finite element model

3 Gating System and Cooling System Design

3.1 Mesh subdivision

The CAD model was transformed into STL format in UG NX and imported into Moldflow software.Firstly, the two-layer mesh is used for meshing. The finite element mesh is composed of three-node triangles, which are created on the outer surface of the model. The grid side length is set to 2mm, the number of nodes is 5378, and the number of grid elements is 10612.Because there are triangles with large aspect ratio in the meshing and the matching degree is less than 90 %, the subsequent analysis results will be affected. Therefore, it is necessary to use the grid repair tool to re-divide the long and narrow grid cells. The repaired finite element mesh is shown in Figure 2. The average aspect ratio is 1.751, the maximum aspect ratio is controlled within 6, and the matching percentage is 92.3%.The mesh orientation is consistent, non-crossed and non-overlapping, which can be used for the next simulation analysis.

3.2 Gating system design

Gating system design is an important part of mold design. The quality of the design can directly affect the quality and service life of the mold. In order to optimize the mold gating system, CAE analysis software can be used to perform preliminary simulation analysis to avoid the failure of mass production or scrapping of the mold due to improper design of the gating system[3]. When analyzing the optimal gate position, it is mainly based on the geometric characteristics and technical requirements of the plastic part,taking into account factors such as the balance of the melt flow, the flow resistance in the cavity and the exhaust conditions[4].Figure 3 shows the simulation results of flow resistance and gate matching. The area indicated in the figure is the area with the smallest flow resistance and the best gate matching. Therefore, the gate position should be designed in the area marked in the figure[5].

Since the cavity layout is symmetrically balanced, in order to save system and analysis time, a partial pouring system model as shown in Figure 4 was designed in Moldflow. Its main technical parameters are:The main channel cone angle is $\alpha = 2°$; The diameter of the circular cross-section of the shunt is d=8mm;The cross-sectional size of the side gate is 2mm×1mm, and the number of occurrences of the runner and gate is set to 2.

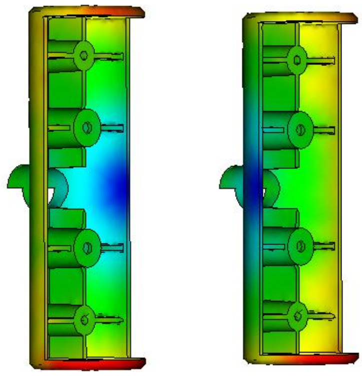

Figure 3 The best gate location

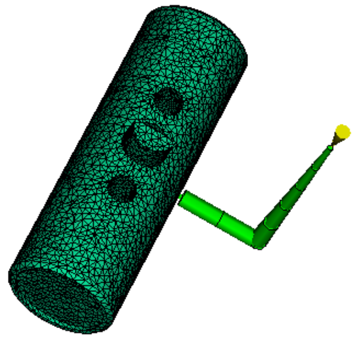

Figure 4 Gating system

3.3 Filling analysis

After the design scheme of the gating system is preliminarily determined, the filling process parameters need to be set. Among them, the mold temperature, melt temperature, injection speed, holding pressure, holding time, cooling time and other variables are very important[6-7].The molding process parameters were set in Moldflow software: the mold temperature was 55 ℃, the material temperature was 235 ℃, the mold opening time was 5s, and the total time of injection, pressure holding and cooling was 30s.

In this paper, the maximum warpage deformation is taken as a reference, and the parameters such as holding pressure and holding time are adjusted many times in combination with the results of flow, holding pressure and warpage analysis.When the maximum warpage deformation of the plastic part is less than 0.5mm, the final combination of process parameters is: the mold temperature is 55℃, the material temperature is 235℃, the holding pressure is 40MPa, the holding time is 10s, and the speed/holding pressure switching time is taken when the filling volume is 100 %. The whole filling process is completed within 1.04 s, and the round table at both ends is the final filling position. The whole plastic part can be filled in a short time, the flow balance is good, and the filling condition is reasonable[8].

Figure 5 shows the temperature simulation results of the flow front. It can be seen from the figure that the temperature difference at the front of the model is less than 1℃, and the color transition is relatively soft, indicating that the melt temperature changes slowly during the filling process, and the melt filling condition is good. It proves that the design of the above gating system is reasonable.

Air pockets may cause the plastic part to be incompletely filled and there will be pores in the part; it may also cause the plastic part to burn and cause scorching. Figure 6 shows the distribution of air pockets. The circles in the figure indicate the locations of air pockets. It can be seen that air pockets are distributed on the boundaries of plastic parts.Parting surfaces, core inserts and ejector pins can be used to connect the gap between the holes is used to achieve the exhaust effect.

Weld lines can cause surface cracks and may also reduce the strength of plastic parts. Figure 7 marks the location of the weld marks on the plastic part. As can be seen from Figure 7,the number of weld marks is small. Combined with the melt flow front temperature analysis results in Figure 5, it can be seen that the temperature difference at the weld marks is small and the fusion is good. The surface quality and mechanical properties of plastic parts are guaranteed.

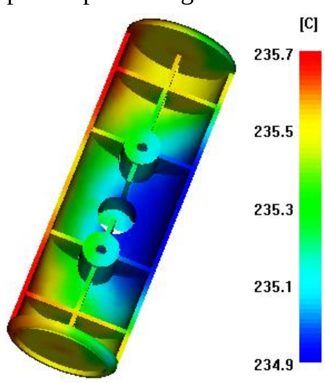

Figure 5 Temperature at flow front

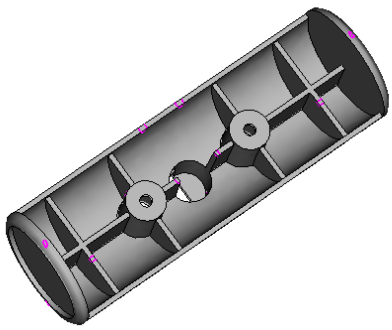

Figure 6 Air traps

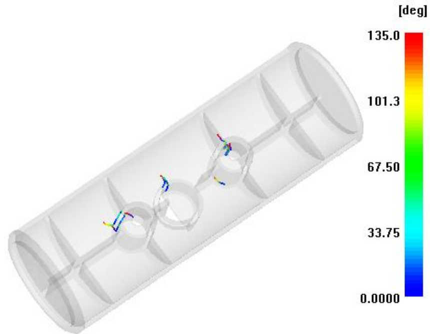

Figure 7 Weld lines

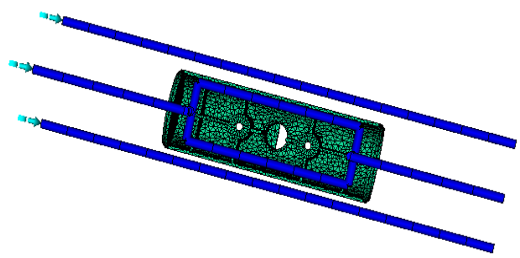

Figure 8 Coolant system

3.4 Cooling system design

First,analyze the structural characteristics of the plastic part. The fixed mold part needs to avoid the central boss.Therefore,a straight-through waterway is distributed on both sides of it, and the distance from the surface of the cavity is kept equal;The intersection of the reinforcing ribs of the movable mold part it is easy to accumulate heat.In order to reduce the temperature difference between the surface of the movable and fixed mold cavities and to avoid structural parts such as push rods, a parallel connection is used to cool the inner surface of the plastic part.The cooling system layout created in Moldflow is shown in Figure 8, and the diameter of the cooling water pipe is 7mm.

3.5 Cooling analysis

Set the cooling medium to water and the inlet water temperature to 25℃. Analyze the above cooling scheme and the results show:

(1) The temperature difference between the outlet

and inlet of the three cooling water channels is less than 1℃;

(2) The extreme temperature difference of the mold is controlled at 30℃, and most temperatures are close to the set mold temperature;

(3) As shown in Figure 9, the round cones on both sides reach the ejection temperature first, and the cooling time at the intersection of the stiffeners is the longest. The time for most areas to reach the ejection temperature is concentrated in about 10 seconds.

To sum up, the flow channel design and flow parameter settings of the cooling system can meet the cooling requirements of the main body of the plastic part.

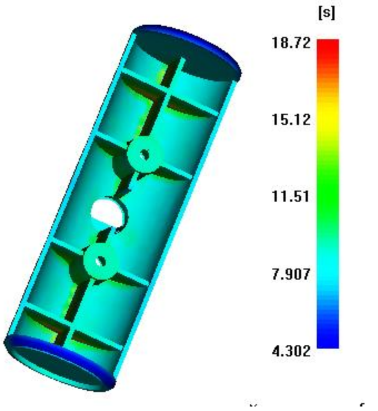

Figure 9 Time to freeze

4 Mold Structure Design

From the perspective of molding, plastic parts can be divided into two parts: the middle part and the two ends. The middle part is more complicated. Considering the processing cost and maintenance and replacement during the life of the mold, combined with the air pocket distribution shown in Figure 6, the three stepped holes are planned to be formed by partial inserts. The two fixed mold inserts and the cavity insert are combined to form the cavity shown in Figure 10, and then the whole is embedded into the fixed mold template; The core structure is shown in Figure 11; Both ends of the plastic part have undercuts. The circular cone of the structure can be formed separately through two side cores.Figure 12 is a schematic diagram of the side core pulling structure.

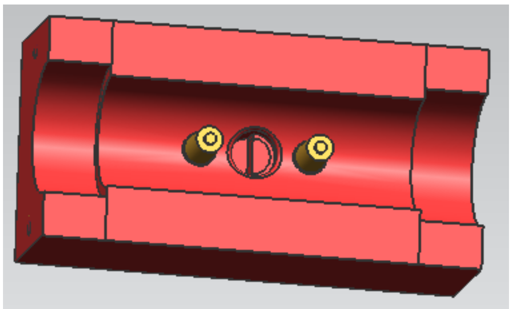

Figure 10 Fixed mold

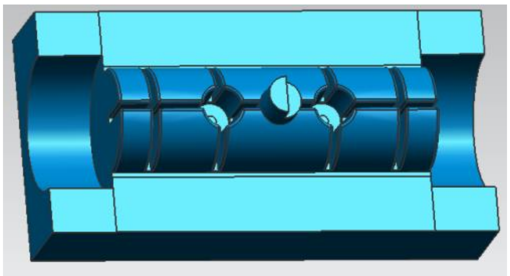

Figure 11 Moving mold

The pushing mechanism uses a push rod, and the pushing position is located at the intersection of the reinforcing ribs.Pay attention to adjusting the assembly clearance between the insert,push rod and hole to ensure the exhaust effect and prevent material spillage.After completing the structural design of each part of the mold, the solid modeling of the entire mold was completed on the Moldwizard module design platform.The mold structure is shown in Figure 13.

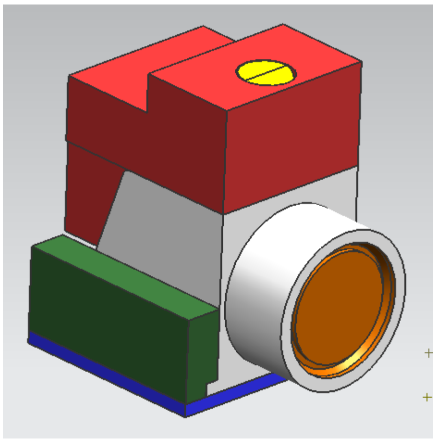

Figure 12 Core-pulling mechanism

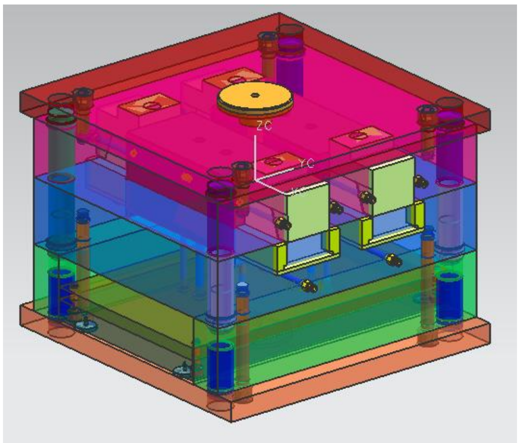

Figure 13 Mold structure

5 Conclusion

(1) Based on the structural characteristics of the plastic parts with support strips, the overall mold design was carried out through the UG-Mold wizard

module. The mold base is a side-pulling core-parting structure with one mold and two cavities.Production practice has proven that the mold structure is reasonable and meets production requirements;

(2) With the help of the mold flow analysis software Moldflflow, it is possible to achieve a substantial improvement in production efficiency, effectively save costs, complete the integration of theory and practice, and provide theoretical guidance and technical support to improve the quality of plastic parts and shorten the production cycle of products;

(3) Using mold CAD technology to quickly and conveniently realize the model design of the entire set of molds, shortening the product development cycle and reducing mold design costs.

Fund Projects: Research Project of Liaoning Provincial Department of Education: JYTMS20230066 — Application of Damping and Vibration Reduction Technology in Key Components of Machine Tools;Yingkou Institute of Technology school-level scientific research project(Grant: ZDIL202302).

Reference

[1] Zhang Liuwei,Gu Saijun,Hong Wei,et al.Design of Large Injection Mould for Automotive Front Frame with Inserts based on CAE Technology[J]. Engineering Plastics Application, 2023,51(2):91-98.

[2] Zhan Yougang. UG NX7.0 Mold Design Tutorial[M]. Bei Jing: Mechanical Industry Press, 2011.

[3] Li Chunling. CAE Technology Based on the Chassis Cover Inverted Injection Mold Design[J]. Plastics, 2020,49(4):50-54.

[4] Qu Huacang. Plastic molding process and mould design[M]. Bei Jing: Higher Education Press, 2005.

[5] Zhao Ertuan, Tian Yujing, Xu Kuan, et al. Injection Mold Design of Fan Cover and Optimization of FormingProcess Based on CAD/CAE[J]. Engineering Plastics Application, 2018,46(10):81-85.

[6] Zhang Jinbiao. Application of injection molding CAE and Moldflow software[M]. Bei Jing: Mechanical Industry Press, 2011.

[7] WU Menglin, ZHANG Long. Parameter Optimization for the Automobile Hood in Injection Molding Based on Orthogonal Method[J]. Plastics, 2009,38(1):5-8.

[8] Chen Hui, Li Mingyao, Wu Huachun. Development of CAD/CAE/CAM technology for mould and its software application[J]. Machinery Design & Manufacture, 2011(6):238-240.

Viser Technology Pte. Ltd.
Mechanical Engineering Science
DOI: 10.33142/mes.v6i2.15055

Research Article Open Access

Research on the Influence of Different Light Intensities on the Characteristics of Solar Cells

Tianlong YUAN*, Sitong HOU, Xidan ZHANG, Peng LI, Dan TANG

Liaoning Provincial Key Laboratory of Energy Storage and Utilization, Yingkou Institute of Technology, Yingkou, Liaoning, 115014, China

****Corresponding Author:*** *Tianlong YUAN, E-mail: yuantianlong@yku.edu.cn*

Abstract

In China, there is a wide range of renewable energy resources, with solar energy resources being the most extensive. Solar cells are devices that directly convert solar energy into electrical energy through the photovoltaic effect. This energy conversion process does not produce any harmful substances that could negatively impact the environment, making solar energy a highly environmentally friendly form of new energy generation. Various external conditions, such as light intensity, light angle, spectral range, temperature, and different materials, can affect the characteristic parameters of solar cells. These parameters include open circuit voltage, short circuit current, maximum output power of solar panels, fill factor, and conversion efficiency. To enhance the longevity and efficiency of solar cells, it is crucial to determine the optimal light intensity for solar cell power generation. This study aims to investigate the patterns of variation in the characteristic parameters of solar cells and their I/V characteristic curves by manipulating light intensity and environmental temperature. The experimental results demonstrate that temperature has an inverse relationship with open circuit voltage, while its impact on fill factor is not significant. Furthermore, the influence of temperature on short circuit current is greatest at 25 ℃ and smallest at 15 ℃.

Keywords: *solar cell; light intensity; ambient temperature; characterization parameters*

1 Introduction

As global economies advance and individuals' living standards improve, there is a concurrent degradation of the global environment. This degradation coincides with an expanding array of new energy sources and a corresponding rise in energy demands. Solar energy emerges as a prominent sustainable energy alternative due to its accessibility and lack of pollutant emissions, particularly into the atmosphere, during its acquisition[1]. Conversely, the combustion of fossil fuels emits pollutants such as carbon dioxide, nitrogen oxides, and sulfur dioxide, exacerbating environmental degradation and the greenhouse effect. Mitigating the emissions of these pollutants is crucial for counteracting the adverse effects on the environment and fostering a habitable ecological setting for human populations.

Governments worldwide are increasingly prioritizing the development of renewable energy sources, with a notable emphasis on solar power generation[2-3]. Solar power generation involves the conversion of solar radiation into electrical energy. Unlike conventional energy sources, this process necessitates only sunlight, obviating the need for additional raw materials. The potential of solar power generation is substantial; estimates suggest that harnessing just 0.1% of solar energy from the Earth's surface, even with a modest conversion efficiency of 5%, could yield a yearly solar power generation output equivalent to 40 times the current global energy consumption[4].

In China, the production cost of polycrystalline silicon for solar photovoltaics has been gradually decreasing, with raw materials now costing around 90,000 yuan per ton. The average comprehensive electricity consumption of the solar photovoltaic power generation industry is approximately 100 TWH/kg[5-6]. The continuous development and improvement of monocrystalline and polycrystalline cell technologies have led to an industrialization efficiency of twenty percent for monocrystalline silicon cells and eighteen percent for polycrystalline silicon cells. Key technologies at the forefront globally include Passivated Emitter Rear Contact (PERC), Heterojunction with Intrinsic Thin layer (HIT), rear electrodes, and high-concentration photovoltaics. In recent years, the cost of solar cell modules in China has decreased to 2.8 yuan/watt, and the investment cost of photovoltaic power generation systems has also dropped to 8 yuan/watt or even less, resulting in a cost of 0.6 to 0.9 yuan/kWh for each unit of electricity, or even less. Promoting large-scale grid-connected photovoltaic power generation projects in China is an ideal choice for changing and optimizing

Received on October 10, 2024; Accepted on November 12, 2024

the power structure, as well as achieving sustainable power supply[7].

2 Experimental Principle

Solar cells are devices that convert solar energy into electrical energy through the photovoltaic effect or photochemical effect.

2.1 Photovoltaic effect

When P-type and N-type semiconductors exist independently, they are both electrically neutral. However, when they are connected together, diffusion occurs. This results in the formation of a P-N junction at the interface of the N-type and P-type semiconductors, as depicted in Figure 1.

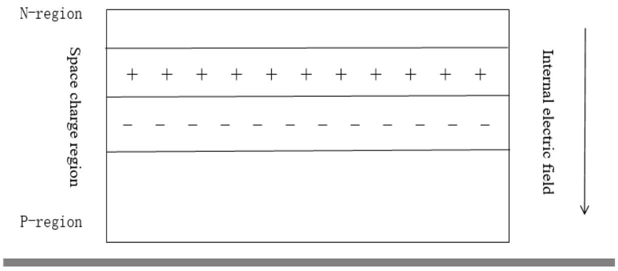

Figure 1 Schematic diagram of P-N junction

When a semiconductor with a P-N junction is exposed to light, the number of electrons and holes within it increases. This causes the electrons in the P region to move to the N region and the holes in the N region to move to the P region under the influence of the local electric field of the P-N junction. Consequently, charge accumulation occurs at both ends of the P-N junction, resulting in the formation of a potential difference. This leads to the creation of a thin layer between the N region and the P region, which in turn generates an electromotive force known as the photovoltaic effect.

In order to efficiently capture solar radiation and separate electron-hole pairs, a potential gradient within the solar cell is necessary. As a result, the materials utilized in the solar cell must possess the capability to absorb the energy of solar photons[4]. Equation (1) describes the relationship between the energy (E) of a photon and its wavelength (1).

$$E = \frac{hc}{\lambda} \tag{1}$$

By substituting the numerical values of the constant h, which is equal to 6.62×10-34 J s, and the speed of light c, which is equal to 3×108 m/s.

Into the formula, we can calculate:

$$E = \frac{1.24}{\lambda} \tag{2}$$

The open-circuit voltage formula in the circuit is represented by equation (3).

$$V_{oc} = \frac{KT}{q}\ln\left(\frac{I_L}{I_o}+1\right) \tag{3}$$

In the formula: IL represents the photocurrent generated in the circuit, measured in amperes (A).

I0 represents the saturation current in the circuit, also measured in amperes (A).

The characteristic resistance formula (4) expresses the ratio between the open circuit voltage (Voc) and the short circuit current (Isc) as follows:

$$R_{ch} = \frac{V_{oc}}{I_{sc}} \tag{4}$$

The formula for the fill factor (FF) in circuits is shown as Equation (5).

$$FF = \frac{Voc \times Isc}{Vm \times Im} \tag{5}$$

In the equations provided:

Voc represents the open-circuit voltage in the circuit, measured in volts (V);

Isc represents the short-circuit current in the circuit, measured in amperes (A);

Vm represents the maximum output voltage in the circuit, measured in volts (V);

Im represents the maximum output current in the circuit, measured in amperes (A).

3 Experimental Process

The solar panels in this experiment are monocrystalline silicon solar panels, with a light-receiving area of 83.5 mm × 60 mm. The experiment is divided into three groups.

(1) Experimental data for solar panels were obtained by conducting experiments at a temperature of 15°C and varying the intensity of illumination, as shown in Table 1.

(2) Experimental data for solar panels were obtained by conducting experiments at a temperature of 25°C and varying the intensity of illumination, as shown in Table 2.

(3) Experimental data for solar panels were obtained by conducting experiments at a temperature of 35°C and varying the intensity of illumination, as shown in Table 3.

Table 1 Experimental data of solar panels at 15 ℃

Light intensity of 15°C	Open circuit voltage V	Short-circuit current mA	Maximum output powerm W	Fill factor
1	1.87	10	13	0.695
1.5	2.02	12	14	0.578
2	2.09	15	15	0.478
2.5	2.11	16	16	0.474
3	2.14	18	16	0.415
3.5	2.15	19	16	0.392
4	2.16	20	16	0.37
4.5	2.16	21	16	0.353
5	2.16	21	16	0.353

Light intensity of 15℃	Open circuit voltage V	Short-circuit current mA	Maximum output powerm W	Fill factor
5.5	2.17	22	16	0.33
6	2.17	22	16	0.33
6.5	2.17	22	16	0.33
7	2.17	23	16	0.32
7.5	2.17	23	16	0.32
8	2.17	23	16	0.32
8.5	2.17	23	16	0.32
9	2.17	23	16	0.32
9.5	2.17	24	16	0.307

Table 2 Experimental data of solar panels at 25 ℃

Light intensity of 25℃	Open circuit voltage V	Short-circuit current mA	Maximum output powerm W	Fill factor
1	1.95	15	19	0.649
1.5	1.95	16	19	0.601
2	2.01	19	19	0.498
2.5	2.05	21	20	0.465
3	2.07	23	20	0.42
3.5	2.09	25	21	0.402
4	2.1	26	21	0.384
4.5	2.11	27	21	0.369
5	2.11	28	21	0.355
5.5	2.11	28	21	0.353
6	2.12	28	21	0.353
6.5	2.12	28	21	0.342
7	2.12	29	21	0.33
7.5	2.12	30	21	0.33
8	2.12	30	21	0.33
8.5	2.12	30	21	0.33
9	2.12	30	21	0.33
9.5	2.12	30	21	0.33

Table 3 Experimental data of solar panels at 35 ℃

Light intensity of 35℃	Open circuit voltage V	Short-circuit current mA	Maximum output powerm W	Fill factor
1	1.97	16	17	0.539
1.5	1.99	17	18	0.532
2	2.02	19	18	0.469
2.5	2.04	21	19	0.443
3	2.06	23	19	0.401
3.5	2.08	24	20	0.4
4	2.08	25	20	0.385
4.5	2.09	26	20	0.368
5	2.09	27	20	0.354

Light intensity of 35℃	Open circuit voltage V	Short-circuit current mA	Maximum output powerm W	Fill factor
5.5	2.10	27	20	0.352
6	2.10	28	20	0.34
6.5	2.10	28	20	0.34
7	2.10	28	20	0.34
7.5	2.10	29	20	0.328
8	2.10	29	20	0.328
8.5	2.10	29	20	0.328
9	2.10	29	20	0.328
9.5	2.10	29	20	0.328

4 Experimental Data Analysis and Conclusions

4.1 Under different light intensity conditions, the curve of the open-circuit voltage of the solar cell panel

The open-circuit voltage of the solar panels was observed at temperatures of 15 ℃, 25 ℃, and 35 ℃, and the results are presented in Figure 2. It was found that the open-circuit voltage increases with the intensity of light, eventually reaching a stable value. The higher the light intensity, the more photons the solar panel absorbs, and the more electrons are generated, which in turn leads to an increase in the concentration of charge carriers and ultimately increases the open circuit voltage. That is to say, the higher the intensity of light, the higher the output voltage of the photovoltaic cell.

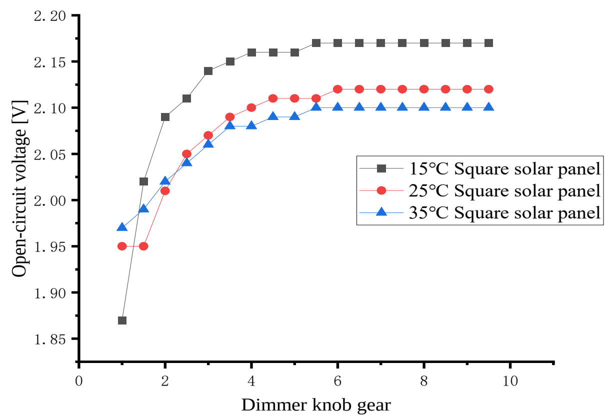

Figure 1 Variation curve of open circuit voltage of solar panel

4.2 Under different light intensity conditions, the short-circuit current curve of the solar cell panel

The short-circuit current of the solar panel can be determined by observing the data at three different temperatures: 15 ℃, 25 ℃, and 35 ℃, as depicted in Figure 2. It is observed that the short-circuit current increases with the rise in light intensity, eventually reaching a stable value. Notably, the highest short-circuit current is recorded at 25 ℃, while the lowest is observed at 15 ℃. This is because the stronger the light intensity, the faster the electron hole recombination at the PN junction interface, resulting in a larger current.

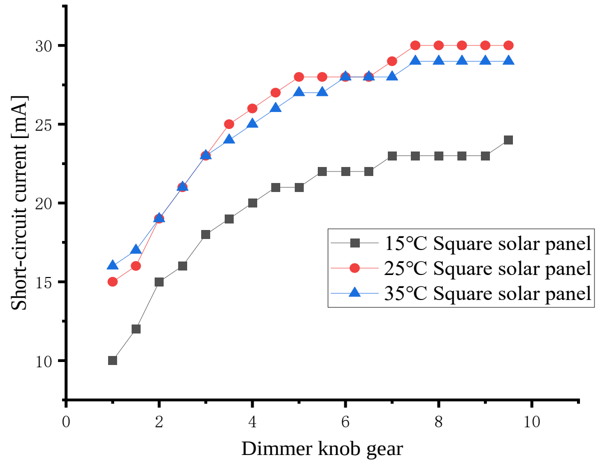

Figure 2 Variation curve of short-circuit current of solar panel

4.3 Under different light intensity conditions, the fill factor curve of the solar cell panel

The observation data for the fill factor of the square solar panel at temperatures of 15 ℃, 25 ℃, and 35 ℃ is presented in Figure 3. It is observed that the fill factor decreases as the light intensity increases, eventually reaching a certain value and stabilizing thereafter. When the light intensity changes, the maximum power point of the battery output will also change accordingly, thereby affecting the size of the filling factor. Generally speaking, the higher the light intensity, the smaller the fill facto.

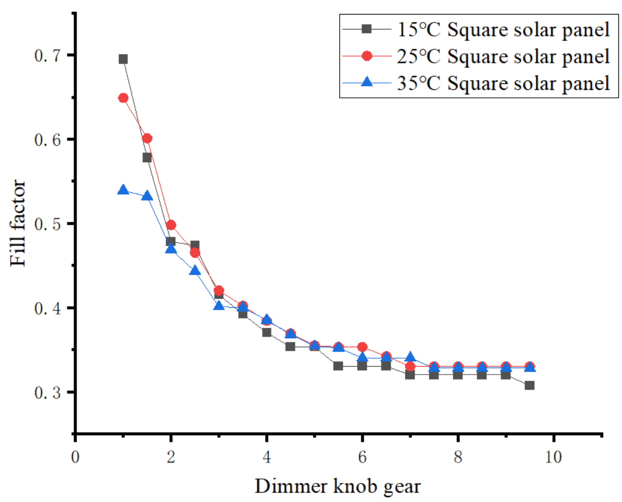

Figure 3 Variation curve of filling factor of solar panel

5 Conclusion

By adjusting the light intensity, the open-circuit voltage and short-circuit current of the solar panel will incrementally rise until reaching a specific value and stabilizing, while the fill factor will gradually decrease with increasing light intensity. The temperature has an inverse proportional effect on the open-circuit voltage, with temperature changes having a less significant impact on the fill factor. Additionally, temperature has the greatest impact on the short-circuit current at 25 ℃ and the smallest impact at 15 ℃.

Fund Projects: The Natural Science Foundation of Liaoning Province of China (Grant No. 2023-MSLH-314), and the 2024 Yingkou Institute of Technology Campus level Scientific Research Project (FDL202408).

References

[1] Wang Heng. Maximum Power Point Tracking Technology and Simulation Implementation in Solar Photovoltaic Power Generation System[J]. Scientific and Technological Innovation, 2022(36):189-192.

[2] Yu Ping. Research on the Characteristics of Solar Cells under Varying Light Intensity[J]. Journal of Jiamusi University, 2022,40(3):146-148,154.

[3] Kumar A S, K N C, Kumar P J, et al. Characteristic Features and Performance Investigations of a PTB7:PC71BM/PFN:Br Pure Organic Solar Cell Using SCAPS-1D[J]. Journal of Electronic Materials, 2023,52(7):4302-4311.

[4] Saeid A, Saeid A K. Additive MXene and dominant recombination channel in perovskite solar cells[J]. Solar Energy, 2022(241):720-727.

[5] Sawalmeha AH W, AlrashdanbSH M,Alashaa'rycMA H.Experimental monitoring system using Arduino microcontroller in studying the effect of temperature and light intensity of solar cell output power in Ma'an development area[J]. International Journal of Smart Grid and Clean Energy (SGCE), 2021,10(2):157-161.

[6] BA F, Ndiaye H E, Faye S, et al. EFFECTS OF LIGHT INTENSITY LEVEL, ILLUMINANCE DEPTH AND TEMPERATURE ON THE PARAMETERS OF A SILICON SOLAR CELL IN CURRENT-GENERATING MODE[J]. International Journal of Advanced Research (IJAR), 2022,10(12):42-45.

[7] Tian D, Weidong X, Shengda X, et al. Light-intensity and thickness dependent efficiency of planar perovskite solar cells: charge recombination versus extraction[J]. JOURNAL OF MATERIALS CHEMISTRY C, 2020,8(36):12648-12655.

Viser Technology Pte. Ltd.
Mechanical Engineering Science
DOI: 10.33142/mes.v6i2.15056

Research Article Open Access

Experimental Study on Classification Method of Leakage Signal in Industrial Boiler Pipeline

Tianlong YUAN, Sitong HOU, Xidan ZHANG, Peng LI, Guangchen XU*

Liaoning Provincial Key Laboratory of Energy Storage and Utilization, Yingkou Institute of Technology, Yingkou, Liaoning, 115014, China

***Corresponding Author:** *Guangchen XU, E-mail: 59701706@qq.com*

Abstract

In this paper, a new acoustic emission detection technology for boiler pipeline leakage using random forest and KNN classifier is proposed. The signal parameter index is processed as feature vector, which overcomes the shortcoming of the traditional method which requires a large number of sample data for training and classification. First, the characteristic parameters of boiler pipeline leakage acoustic emission signal are extracted, and then the extracted characteristic parameters are input into random forest and KNN classifier as feature vectors for classification processing. Eight indexes including amplitude, ringing count, duration, energy, rise count, rise time, RMS voltage and average signal level are selected and input into the classifier as feature vectors. As a diagnostic for pipeline leak classification. The experimental results show that this method is effective and feasible in pipeline leak diagnosis, and the feasibility of applying random forest and KNN algorithm to the classification of acoustic emission signals in pipeline leak detection is verified.

Keywords: *pipeline; leakage signal; algorithm; detection*

1 Introduction

Acoustic Emission (AE) refers to the physical phenomenon that when a material is subjected to local deformation or external force, it quickly releases elastic energy and generates transient stress waves, also known as elastic wave emission. At present, according to the characteristics of pipeline leakage detection, the commonly used methods mainly include negative pressure wave method, pressure point analysis method, mass/volume balance method, etc.[1], among which negative pressure wave method has better sensitivity and accuracy, low cost, and can reduce the false alarm rate by using a lower threshold value. However, its shortcomings lie in the fact that it requires sudden and massive leakage. If there is a small slow leak in the pipeline, it is difficult to detect, resulting in a failure of diagnosis[2-3]. Acoustic emission technology has its own advantages compared with traditional non-destructive testing methods: first, the material itself emits defect information, rather than external equipment to supply its energy; Thirdly, the existing leakage can be continuously detected, and the requirement for real-time diagnosis is not high. The leak signal is not required to be detected when the leak just occurs, but can be detected after a period of time when the leak occurs, which greatly improves the convenience and correctness of diagnosis[4]. Acoustic emission technology has been widely used in aerospace, petrochemical, railway, automobile, construction, electric power and other fields. Industrial waste heat boiler works in extremely harsh environment, the medium in the tube is high temperature and high pressure fluid, and the outside of the tube needs to withstand the radiation and convection heat transfer of high temperature flue gas and continuous erosion of ash particles, so it is more prone to leakage accidents. Leakage generally does not suddenly occur in a large area, the initial leak development is slow, non-destructive leakage, after a few days or weeks, to a certain extent will become destructive leakage.

At present, online acoustic monitoring technology is mainly used in China[5]. This method is to open an air acoustic propagation hole on the wall of the furnace tube, weld an air acoustic waveguide on the propagation hole and install an air acoustic sensor. In order to master this advanced detection technology, an acoustic emission sensor was installed on the boiler in the laboratory, and the pipeline leakage and noise were simulated by lead breaking, percussion and sandpaper friction[6]. The acoustic emission signals were classified by random forest and KNN algorithm, and the leakage signals were effectively identified. It lays a foundation for the application of acoustic emission technology in pipeline leakage of industrial boilers[7]. The operation parameters of industrial boiler system are numerous and affect each

Received on September 8th, 2024; Accepted on October 16, 2024

other, and some parameters that can directly reflect the operation of boiler are often difficult to measure. Therefore, we need to find a new fault diagnosis method to monitor the boiler system in real time and get the expected results.

2 Basic Principle of Classifier

2.1 Random forest classifier

2.1.1 Definition of random forest classifier

A random forest is a classifier that uses multiple trees to train and predict samples, uses a recursive method to generate many trees, and then votes on the results to determine the sample category. Each tree is constructed independently by randomly extracting samples from the training data set. Because random forest uses the method of randomly selecting features at each node, the correlation between trees in the forest is reduced, and the error rate is reduced.

2.1.2 The construction process of random forest classifier

(1) Select some samples and features randomly from the sample set;

(2) Train a decision tree using selected samples and features;

(3) Repeat step 1 and Step 2 several times to build multiple decision trees;

(4) For each sample, the classification result of each decision tree is voted, and the classification result with the most votes is selected as the final result.

2.1.3 Advantages and disadvantages of random forest classifier

Advantages:

(1) Random selection of features and samples reduces the risk of overfitting;

(2) It can process high-dimensional data without the need for feature selection;

(3) Can deal with missing values and outliers;

(4) The importance of each feature can be assessed for feature selection and interpretation models.

Disadvantages:

(1) The training time of random forest classifier is longer than that of a single decision tree, so multiple decision trees need to be built.

(2) The model of random forest classifier is complex and difficult to explain.

2.2 KNN classifier

2.2.1 Definition of KNN classifier

K-nearest Neighbor (KNN) algorithm is a commonly used supervised learning method, originally proposed by Trevor Hastie. The idea of the algorithm is that for a given sample d, K Nearest Neighbor samples are found by calculating the distance, and the category of sample d is the category that most of the samples belong to.

2.2.2 Workflow of KNN classifier

(1) Collect data: collect sample data of known categories;

(2) Calculation distance: Calculate the distance between the sample to be classified and the sample of the known class, usually using Euclidean distance or Manhattan distance;

(3) Select K value: Select the nearest K known class samples;

(4) Determine the category: according to the category of K nearest neighbors, determine the category of the sample to be classified. The majority voting method is usually adopted, that is, the category with the most occurrences among the K nearest neighbors is selected as the category of the samples to be classified.

2.2.3 Advantages and disadvantages of KNN classifier

Advantages:

(1) The theory is mature and the thought is simple, which can be used to do classification or regression;

(2) Can be used for nonlinear classification;

(3) The training time complexity is lower than that of other algorithms such as support vector machines, only O(n);

(4) Compared with naive Bayes and other algorithms, there are no assumptions about the data, high accuracy and insensitive to anomalies;

(5) Because KNN method mainly depends on the limited neighboring samples, rather than the method of discriminating the class domain to determine the category, KNN method is more suitable for the sample set with more crossover or overlap of class domains;

(6) The algorithm is more suitable for the automatic classification of class domains with large sample size, and those class domains with small sample size are more prone to misclassification by using this algorithm.

Disadvantages:

(7) Large amount of calculation;

(8) The problem of sample imbalance (i.e., some categories have a large number of samples, while others have a small number of samples);

(9) Requires a lot of memory.

3 Evaluation Standard

For evaluating and detecting the performance of boiler leakage signal system, it is usually divided into True Positive example, False Positive example and true negative example according to the combination of its real category and the prediction category of intrusion detection system.In the four cases of (True Negative) and (False Negative), the Precision is calculated according to the following formula (1) to evaluate the performance of the boiler abnormal detection system.

$$\text{Precision}=\frac{TP}{TP+FP} \tag{1}$$

4 Experiment

First, the boiler data is standardized, and then the features are extracted by empirical wavelet transform, and the parameters of the AR model are estimated by selecting the features with large information content. By adjusting the order p, AR models under different orders are obtained. Finally, various classifiers are used to predict the intrusion data.

Three types of simulated leakage acoustic emission signals were obtained by tapping, sandpaper friction and lead breaking on laboratory boiler pipes. By analyzing the time-domain waveform and frequency spectrum of the three types of acoustic emission signals, random forest and KNN algorithm were used to analyze the characteristic parameters of the leakage signals. Eight indexes, including amplitude, ringing count, duration, energy, rise count, rise time, RMS voltage and average signal level, were selected and input into the classifier as the diagnosis of pipeline leakage classification to verify the feasibility of applying random forest and KNN algorithm to the classification of acoustic emission signals. Specific parameters are shown in Table 1.

In order to verify the stability of the algorithm, the K-fold cross-validation method is used for experiments. The basic idea of K-fold cross-validation is to divide the original data into k groups, take turns taking group K-1 as the training set, and the remaining group as the test set. k tests are repeated to obtain k classification models, and the final results of these k models are averaging, so as to analyze the performance of the algorithm. In this experiment, the value of k is 3. In this chapter, two parameters are used to test the effectiveness of the algorithm, namely the order p of the AR model and the internal parameters of the classifier. For the AR model, the order p is taken from 2 to 8. For a random forest, the parameter RF takes the value 1,2,3,4,5. For KNN, the values of parameter k are 1,2,3,4,5. Figure 1 shows the precision values of various attack types when random forest and KNN classifier are used.

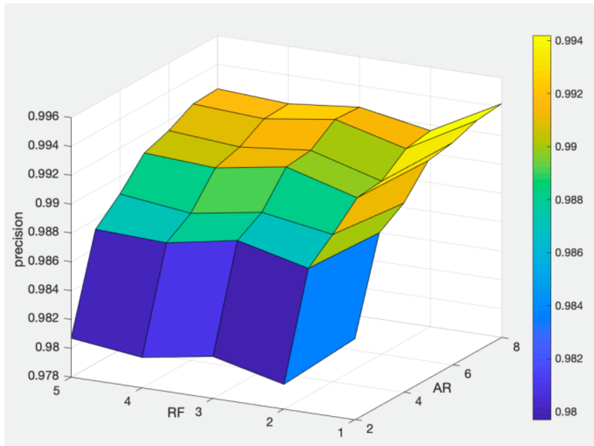

Table 1 The training and testing data

Category	Range	Ringing count	Duration	Energy	Rise count	Rise time	RMS	ASL
1	85.6	1606	74837	22464.3982	84	2006.5	0.761	49.5
1	83.8	1258	50542	10079.3015	116	2116	0.632	46
1	83.8	1525	69005	16824.2737	64	1958.5	0.624	47.7
1	83.9	1073	48143.5	11045.0485	92	2020	0.733	47.2
1	82.9	1381	55881	9138.7009	56	1945.5	0.503	44.3
2	80.1	8086	138328.5	100970.4834	3510	37337	1.206	57.3
2	82	11282	195532	138810.8475	7832	87377.5	1.321	57
2	77	8819	188334	96524.1531	5171	92933.5	0.888	54.2
2	72	8323	148967.5	49133.5358	4917	65165.5	0.531	50.4
2	77.1	12334	196223	93520.4971	8038	96712	0.823	53.6
3	89.8	4455	103773.5	118017.1829	59	474.5	2.503	61.1
3	85.8	4157	91367	68001.5442	61	473.5	1.578	57.4
3	85.3	4464	90805	70743.3914	66	473.5	1.654	57.8
3	86.5	4986	94894.5	89484.1476	812	7328	1.976	59.5
3	86.4	4456	85698	67500.8041	67	473.5	1.663	57.9
1	87.9	1791	84824.5	28623.2269	61	1972	0.93	50.6
1	87.8	1696	80705	27050.116	62	1983	0.912	50.5
2	81.3	10798	176710	106503.9536	6282	74547	1.068	55.6
2	81.7	10451	159592.5	111884.9625	5241	51598	1.205	56.9
3	83.8	4783	85828.5	54494.8898	68	474	1.33	56.1
3	89.5	4963	117936.5	118972.7081	482	17246.5	2.391	60.1

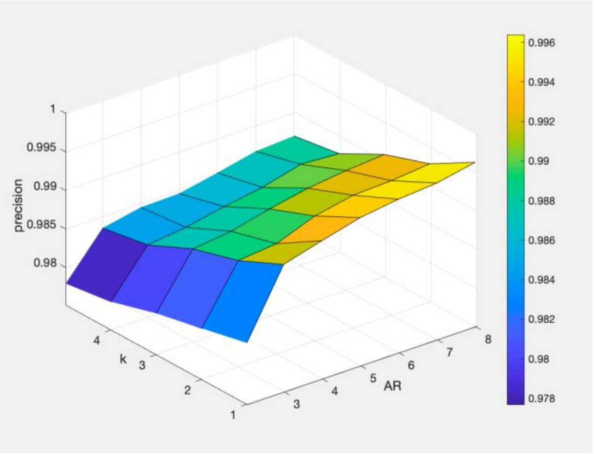

Figure 1 Random forest and KNN classifier accuracy variation with AR

As can be seen from Figure 1, for the random forest classifier, with the increase of AR value, the decrease of k value, the higher the accuracy; For KNN classifier, with the increase of AR value and the decrease of k value, the accuracy is higher. When both the random forest classifier and KNN classifier take k to 8, the results tend to be stable.

5 Conclusion

Acoustic emission testing technology is a dynamic non-destructive testing method, which has many advantages and characteristics that traditional testing methods can not compare. Based on this, this paper proposes to extract the characteristic parameters of acoustic emission signals of boiler pipeline leakage, and then input the extracted characteristic parameters into random forest and KNN classifier as feature vectors for classification processing. 8 indicators are selected to form feature vectors and input into the classifier, so as to successfully identify different kinds of acoustic emission signals. The feasibility of applying this method to the classification of boiler pipeline leakage signals is verified.

Fund Projects: The Foundation of Liaoning Provincial Key Laboratory of Energy Storage and Utilization (CNNK202406), and Yingkou Institute of Technology campus level research project — Development of food additive supercritical extraction equipment and fluid transmission system research.

References

[1] WANG Zhao-hui, ZHANG Lai-bin, XIN Ruo-jia, Application of acoustic emission technique in pipeline leakage detection[J]. Journal of the University of Petroleum China(Edition of Natural Science), 2007,31(5):87-90.

[2] WANG Zhao-hui, ZHANG Lai-bin. Research of small leakage diagnostic technique for liquid delivery pipeline [J]. China Petroleum Machinery, 2003,31(8):37-40.

[3] LIANG Wei, ZHANG Lai-bin, WANG Zhao-hui. State of research on negative pressure wave techniques applied to leak detection in liquid pipelines[J]. Pipeline Technique and Equipment, 2004(6):16-19.

[4] JIAO Jing-pin, HE Cun-fu, Wu Bin. Advance in acoustic emission techniques for pipeline leak detection[J]. Nondestructive Testing, 2003,25(10):519-522.

[5] Ma Liangyu, WANG Bingshu, TONG Zhensheng. Fuzzy recognition and Neural Network Method for Fault Diagnosis of condenser[J]. Proceedings of the CSEE, 2001,21(8):68-73.

[6] Wang Ming-hui.The application of digital temperature sensor DS18B20 in the measuring of the chemical industry[J]. Computers and Applied Chemistry, 2007,24(9):1249-1252.

[7] Yang Hongying, Hua Ke, Ye Hao, et al. Study of the leak diagnosis based on acoustic signal for gas pipelines[J]. Computers and Applied Chemistry, 2010,27(8):1009-1012.

Publisher: Viser Technology Pte. Ltd.

URL: www.viserdata.com

Add.:111 North Bridge Rd, #21-01 Peninsula Plaza,

Singapore 179098

ISSN 2661-443X